Diseño de un modelo computacional que permita identificar la influencia de las cargas mecánicas en la morfogénesis de articulaciones sinoviales.

Andrés Felipe Carrera Pinzón

Facultad de Ingeniería

Bogotá, Colombia

2019

UNIVERSIDAD NACIONAL DE COLOMBIA
SEDE BOGOTÁ

Design of a computational model that allows identifying the influence of mechanical loads on the morphogenesis of synovial joints.

Andrés Felipe Carrera Pinzón

Faculty of Engineering

Bogotá, Colombia

2019

Design of a computational model that allows identifying the influence of mechanical loads on the morphogenesis of synovial joints.

Research work presented as a requirement for the degree of:

Maestría en ingeniería – Ingeniería Mecánica

Advisor: Diego Alexander Garzón Alvarado, Ph.D.

Co-Advisor: Kalenia Márquez Flórez, M.Sc.

Department of Mechanical Engineering and Mechatronics

Research line: Mechanobiology- Computational Mechanics

Research group: Mathematical Modelling and Numerical Methods (GNUM)

Universidad Nacional de Colombia

Faculty of Engineering

Department of Mechanical and Mechatronics engineering

Bogotá, Colombia 2019

Content

Abstract 1

1. Introduction 3

2. Objectives 8

2.1. General Objective 8

2.2. Specific objectives 8

2.2.1. SOB-1 8

2.2.2. SOB-2 8

2.2.3. SOB-3 8

3. Background 9

3.1. Experimental works on embryo and fetal development 10

3.2. Computational works 12

3.3. Ossification process (Osteogenesis) 13

4. Material and Methods 15

4.1. Biological variables 15

4.2. Mathematical model with the Finite Element Method (FEM) 17

4.2.1. Boundary conditions 17

4.2.2. Translated and rotated elements 18

4.2.3. Biological growth 19

4.3. Modelled cases 20

4.4. Ossification Process 21

5. Results 24

5.1. Normal joint morphogenesis model 24

5.2. Pathological joint morphogenesis models 27

5.3. Endochondral Ossification 31

6. Discussion 33

7. Conclusions 38

8. References 40

9. Annexes 45

List of Figures

Figure 1. Joint classification according to their function [authors modified from [1]] 3
Figure 2.Limb formation and mesenchyme cell distribution [Authors]. 4
Figure 3. States of synovial joint development [Authors]. 5
Figure 4. Synovial joint components [1], [3]. 9
Figure 5. General types of a synovial joint in the human body. [Adapted from [1], [3]] 10
Figure 6. Osteogenesis process [Adapted from [1], [3]]. 14
Figure 7. Process of the joint onset development. 16
Figure 8. Results of the biochemical distribution over the two opposite rudiments in the last time step of the model [9]. 17
Figure 9. Boundary condition implemented on the model [Authors]. 18
Figure 10. Translation and rotation of the centroid elements of each rudiment [Authors]. 19
Figure 11. The geometry of the pathological kilter model [Authors]. 21
Figure 12. Morphogenesis of interphalangeal joint [Authors] 24
Figure 13. Stress distribution of the computational model at different time steps [Authors] 25
Figure 14. Molecular distribution for the joint morphogenesis. [Authors] 26
Figure 15. Results of the first case of the pathological model. [Authors] 27
Figure 16. Mechanical stress distribution in the first pathological case. [Authors] 28
Figure 17. Joint morphogenesis of the second pathological case. [Authors] 28
Figure 18. Results of the pathological joint morphogenesis models [Authors] 29
Figure 19. Mechanical stress distribution in the pathological models [Authors] 31
Figure 20. Representation of the POC and SOC by the OI [Authors] 32
Figure 21. Comparison with an x-ray phalanx and the result from the joint morphogenesis computational model [Authors] 34
Figure 22. Total comparison between normal and pathological models [Authors] 35
Figure 23. Comparison with a schematic draw of the Secondary Ossification Centers (SOC) [Authors] 36
Figure 24. Infinitesimal element considering ($\Delta x \approx \Delta y \approx 0$) and ($\Delta z = 1$) [Authors] 45
Figure 25. Quadrilateral element with the corresponding nodal displacement $u(x, y)i$ [Authors] 47
Figure 26. Quadrilateral reference element in the new coordinate system (ξ, η). 49
Figure 27. Newton Raphson diagram to explain ABAQUS software solution procedure [Authors] 53

Table of symbols and abbreviations

Symbol	Name	Value	Unit
E	Young modulus	Depends on the variable	kPa
μ	Poisson ratio	0.49^{*}	-
H	Hydrostatic stress	Depends on the variable	kPa
VM	von Mises stress	Depends on the variable	kPa
$Shear$	Shear stress	Depends on the variable	kPa
$PTHrP$	Parathyroid hormone-related peptide	Depends on the variable	-
Ihh	Indian Hedgehog homolog	Depends on the variable	-
Wnt	Wnt protein	Depends on the variable	-
Hox	Hox gene	Depends on the variable	-
OI	Osteogenic index	Depends on the variable	-
POC	Primary ossification center	Depends on the variable	
SOC	Secondary ossification center	Depends on the variable	-
K_1	Constant weight for proximal phalange	Depends on the variable	-
K_2	Constant weight for distal phalange	Depends on the variable	-
θ	Theta	0, 30, 60, 90	Degree (°)

d^{growth}	Strain tensor	-	-
δ_{ij}	Delta-Kronecker tensor	$1\ if\ i = j$ $0\ other\ case$	-
$\otimes$	Tensorial product	-	-
TH_{PTHrP}	A threshold value for PTHrP	≥1.1	-
TH_{WNT}	A threshold value for WNT	≥0.01	-
$\boldsymbol{\sigma}$	Stress tensor	-	-
$\boldsymbol{D}$	Material tensor properties	-	-
$\boldsymbol{\epsilon}$	Strain tensor	-	-

List of Tables

Table 1. Maximum and minimum values of the molecular parameters included in the mechanobiological model [9]..... 17
Table 2. Conditions of normal and pathological cases modelled [Authors] 20
Table 3. Numbers of points and weights for numerical integration using Gauss quadrature in rectangular elements[42] 52

Abstract

Synovial joints enable the relative movement between the connected bones. The lubricated articular cartilage and the shape of the joint facilitate and soften the relative displacement of the joint's parts. These joints, their development process involves a series of steps, they begin from the bone blastema and differentiate into chondrocyte, after this, appears the physical separation, and finally, occurs the joint shaping. However, the process of how these joints obtain their final shape is yet not well understood. Former models have been developed in order to understand the joint morphogenesis considering only the mechanical environment, but the obtained shape is not entirely correct. In this study, a computational model was developed with the aim to explain how the morphogenesis of these joints is achieved. For this model both, the mechanical and molecular environments, were considered.

This model applies the finite element method to describe how, during the fetal stage, two opposite segments of bone cartilaginous rudiments of a synovial joint shape. It was assumed that cyclic hydrostatic stress affects cartilage growth in a positive way, also, that the concentration of molecules, such as PTHrP and Wnt, promote chondrocyte proliferation hence cartilage growth. With these considerations, the morphogenesis of an interphalangeal joint was modelled.

For the simulation, four stages of rotation were considered, in each of them the distal phalanx had an angle with respect the proximal phalanx, the angles were 90°, 60°, 30° and 0°. Moreover, it was considered six (6) pathological cases for joint morphogenesis: a kilter model (dislocation), a model without the molecular influence, and a 0° and 90° palsy models with and without molecular influence. In addition, in the normal model were predicted the shapes of the primary and secondary ossification centers (POC and SOC) by calculating the osteogenic index (OI), which was dependent on the concentrations of PTHrP-Ihh.

The obtained results show a coherent final shape of an interphalangeal joint, and the shapes of the POC and SOC computed through the OI were similar to schematic drawings of the ossification centers. Furthermore, the pathological cases show us an abnormal behavior of the joint morphogenesis that might be related to developmental joint diseases.

The results suggest that the mechanical and the molecular environment are crucial to the joint morphogenesis. This process involves a relationship between the hydrostatic stress and molecular concentrations, with cartilage growth and chondrocyte proliferation. This leads us to a new understanding of prenatal joint development.

Keywords: Synovial joint, Morphogenesis, FEM, Joint development, Cartilage growth, Joint

1. Introduction

Joints, anatomically, are the locations where two bones connect to each other. These joints allow lower, high or no movement between bones without losing stability. The joints can be classified according to their structure or their function [1]. The structure classification is related to how the bones are connected, and they can be further classified as fibrous (the bones are connected by a fibrous tissue), cartilaginous (the bones are connected by hyaline or fibrocartilage tissue) and synovial joints (the bones are not connected and the bone surfaces are coated by hyaline cartilage), which are composed by different structures, such as cartilage, ligaments, and synovial and fibrillary capsule, an examples of this kind of joints are the hip or knee joints [2], [3].

On the other hand, the function classification divides them according to the degree of movement of the joint into synarthrosis (low movement joints, and can be either fibrous or cartilaginous joints) (Figure 1-A), amphiarthrosis (medium movement joints, and can be either fibrous or cartilaginous joints) (Figure 1-B), and diarthrosis (high movement joints, synovial joints) (Figure 1-C) [1]–[3].

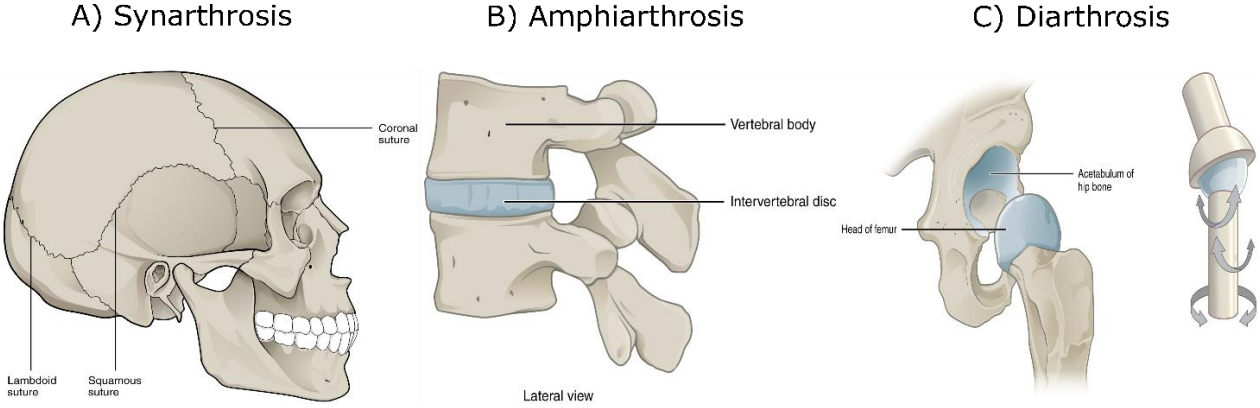

Figure 1. Joint classification according to their function [authors modified from [1]]

A). Synarthrosis joint. Suture Joints of Skull. B). Amphiarthrosis joint. Intervertebral disc. C) Diarthrosis (synovial) joint. An example, the hip joint [1]–[3].

The joints formation occurs during the embryonic stages of development in conjunction with the formation and growth of the associated bones. The mesenchyme cells are the precursors of bones, cartilages and connective tissues of the body [1], [4], [5]. The limbs initially develop as small buds (Figure 2), each bud continues to grow and elongate during development, within the buds are areas of condensation mesenchyme cells (cluster of cells) which begin to differentiate into chondrocyte that will form the future bone anlagen and joints [1], [6] (Figure 2).

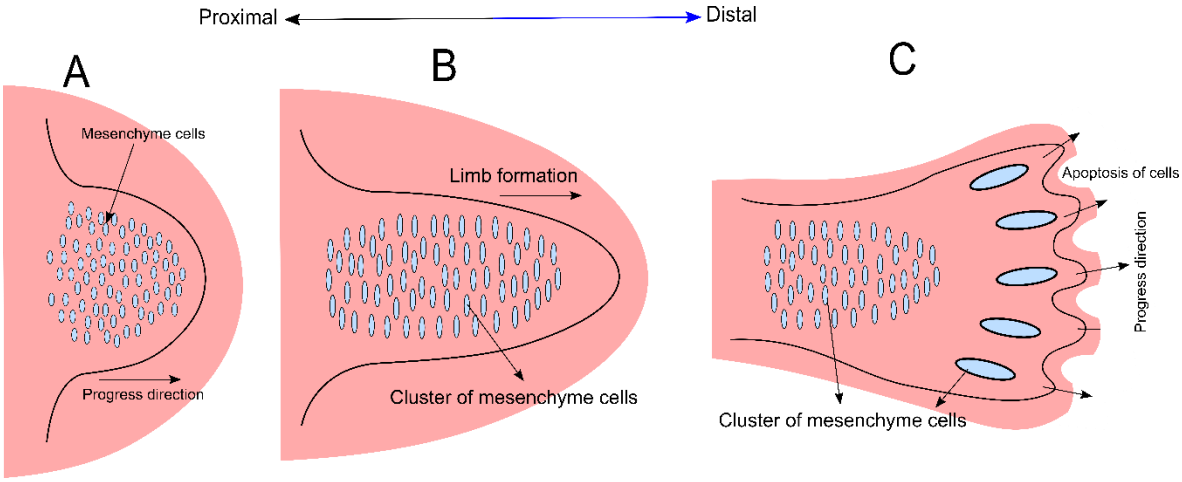

Figure 2.Limb formation and mesenchyme cell distribution [Authors].

A. The small bud starts to form by the condensation of mesenchyme cells. B. The direction of limb formation and mesenchyme cells defined (cluster cells). C. Extremity formation with mesenchyme cell diffusion distribution (distal section) and the cluster of mesenchyme cells. [Authors]

Once the cluster of cells has defined the bone blastema (Figure 3), initiates the joint development process, which is characterized by three stages: the Interzone onset, cavitation process, and morphogenesis. The Interzone onset determines the joint position within the bone blastema and it is characterized by cells that have stopped their differentiation into chondrocytes [7], [8]. The Interzone gives place to the cavitation process which leads to the physical separation of the anlagen [8]. And finally, the joint molds to its final shape (morphogenesis) after the cavitation process (Figure 3).

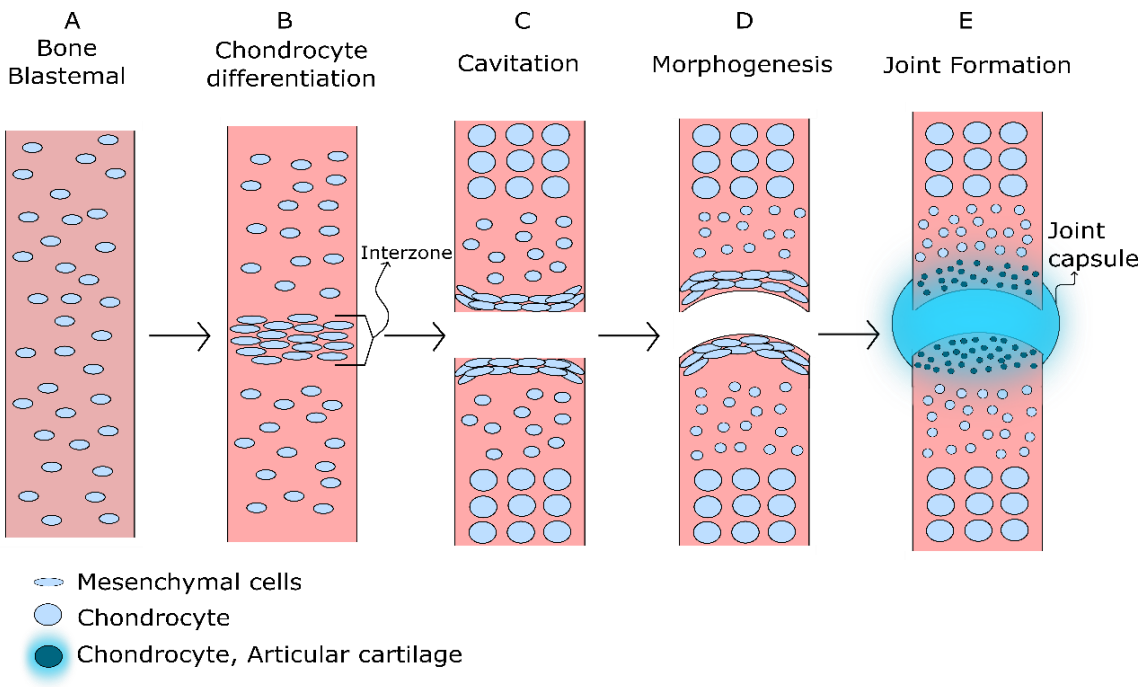

Figure 3. States of synovial joint development [Authors].

A) Bone blastemal, mesenchymal cells condensed in the first stage. B) Interzone forms at the site of the joint where mesenchymal cells have not differentiated into chondrocytes. C) The cavitation process leads to the physical separation of the anlagen and forms the synovial cavity. D) The morphogenesis process starts shaping the opposite sites of the rudiments. E) Distinct components developed as mature joint. [2, 5, 6]

Once the bone cartilaginous rudiments have formed, they start their ossification process (endochondral ossification) in which the chondrocytes in the center of the mold begin to growth in size and their ECM start to calcify. This produce that the chondrocyte stops receiving more nutrients, which cause their apoptosis, leaving a space within the bone due to the disintegration of the surrounding cartilage. Moreover, blood vessels invade the empty space carrying osteogenic cells (which becomes osteoblasts), marking the onset of the primary ossification center (POC) [1]. The presence of osteogenic cells initiates the transformation of the perichondrium into osseous tissue, forming the periosteum (a collar around the diaphysis). This process continues while the cartilage at the end of the bone (epiphyses) keeps growing. After birth, the same process of matrix mineralization, chondrocyte apoptosis, and blood vessel invasion occur at the epiphyses of the bone, creating the secondary ossification center (SOC) [1], [6], [8].

There is another type of ossification process which occur mainly in flat bones. For example, in the head, the mesenchyme will accumulate at those areas that will become in bones, and form the top and sides of the skull (Figure 1-A). The mesenchyme differentiates within these areas directly into the bone (osteoblasts), through the process of intramembranous ossification [1], [3].

In the decades of fifty´s, Ernest Gardner (1950) was the first author that described and identified that during embryonic stages exist and interaction between biochemical (molecular) and mechanical stimuli [11]. Future researches were oriented to evaluate the molecular and mechanical interaction in the embryonic stages, such as molecular activity, tissue characterization, bone formation, and articular degenerative problems [11]–[17]. These works were made with the aim of identifying and proposing solutions for a diverse number of joint diseases at different stages of development.

A developmental disease that is commonly diagnosed and occurs during embryo stages is the developmental dysplasia of the hip (DDH), a congenital condition of the hip joint [18]–[20]. Some studies have researched the real cause of DDH, but is still not known, however, they presented an anatomical definition that refers to inadequate development (genetic and environmental) of the acetabulum, or the femoral head, or both [19]–[21].

Furthermore, there exists another developmental disease that is related with the joint contracture and the abnormal fibrosis of the muscle tissue, causing muscle shortening and therefore the individual is unable to perform active extension and flexion in the affected joint. This disease is known as arthrogryposis and is described as a congenital joint contracture (palsy) in different areas of the body [18], [19], [21], [22]. This disease can be divided into three groups, the amyoplasia, distal arthrogryposis and the syndromic. Amyoplasia is characterized by severe joint contracture and muscle weakness. The distal arthrogryposis, when it occurs in hands and feet. While the syndromic is a type of arthrogryposis which involves neurological and muscle diseases [18], [19], [21], [22].

These previously mentioned diseases can occur during the prenatal stages, whereas there exist other types of diseases that affect mature joints, i.e. a cartilage degenerative diseases such as arthritis and osteoarthrosis [23]. Arthritis generates symptoms as swelling, pain, stiffness and decreased range of motion. Sometimes the pain can be mild, moderate or severe. Arthritis can cause permanent joint changes [23]. On the other hand, in the osteoarthrosis, the cartilage cushioning surface on the ends of bones wears away, the bones rub against each other, causing pain, swelling and stiffness. Over time, joint pain may become chronic [23].

The mentioned diseases are the result of diversely causes and disorders like mechanical action, molecular stimulus (hormonal), excessive use of the joint, or even an accident. However, medical science has developed treatments based on biophysics stimuli and drugs implementation, to active-inhibit the molecular response that causes pain and inflammation of the affected area [18]–[22].

For this study was designed a 2D finite element model of two opposite bone rudiments of an interphalangeal joint, including the synovial capsule. This computational model considers the molecular and mechanical interaction on the joint morphogenesis process. We started from the cavitation stage to the final shaping of the joint and analyzed the shape of the POC and SOC that was predicted with the Osteogenic Index (OI). The initial geometry of the two opposite pieces of cartilage and the molecular parameters (PTHrP, Wnt, Hox, and Ihh) were extracted from the results of a previous study of our research group [9].

This work presents a computational model of normal synovial joint morphogenesis, and also some pathological cases of joint morphogenesis. This work is divided in introduction, objectives, background, materials and methods, results, a discussion chapter, and finally, the conclusions of the study. The introduction contains a brief description of synovial joints, developmental joint diseases and articular diseases. The background chapter explains the experimental and computational researches found in literature, a review of the osteogenesis process, and a brief explanation of the finite element method. In the materials and method chapter, it is explained the molecular variables that were considered to interact in the joint formation, more specifically, during the morphogenesis process. Furthermore, it presents the mechanical model that was implemented (Boundary conditions), a section of the pathological cases studied, and the shapes of the ossification structures computed by the osteogenic index (OI). The results chapter shows the obtained shapes of the joint and the POC and SOC through the computational model. Subsequently, comes the discussion of the obtained results and their comparison to what was found in the literature. At the end of the document is the concluding chapter which is shown what can be concluded from the work.

2. Objectives

2.1. General Objective

Determine, in silico, the effects of the mechanical loads during the morphogenesis of synovial joints during the fetal state.

2.2. Specific objectives

2.2.1. SOB-1

Stablish the mechanobiological factors involved in the morphogenesis of synovial joints

2.2.2. SOB-2

Formulate a mathematical model to represent the mechanobiological behavior during the morphogenesis of synovial joints.

2.2.3. SOB-3

Develop of a computational model to determine the influence of mechanical loads in the articular morphogenesis

3. Background

In this chapter, we present a literature review of some aspects of the synovial joints, the endochondral ossification, and we describe some research work and mathematical models found in the literature that addresses to explain the joint morphogenesis and ossification process. Moreover, we included a brief description of the Finite Element Method (FEM).

The synovial or diarthrosis joints are composed by cartilage, ligaments, and the synovial and fibrillary capsule (Figure 4). These joints are further classified into six different categories (planar, hinge, pivot, condyloid, saddle, ball and socket) based on their shape and structure, which determine the type of movement allowed by the joint (Figure 5).

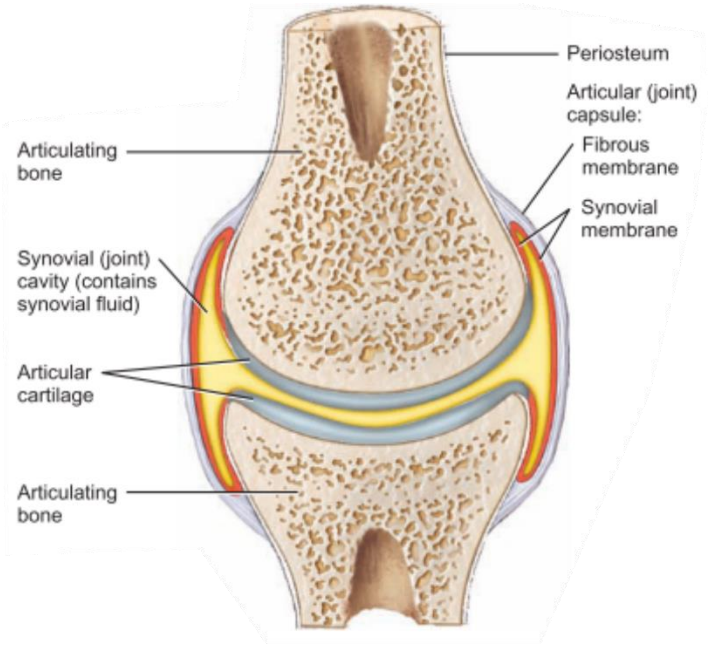

Figure 4. Synovial joint components [1], [3].

The synovial joint allows for movements for smooth movements between adjacent bones. Joint surrounded by an articular capsule that defines joint cavity filled with synovial fluid. Ligaments support the joint holding the bones together. The articular surfaces of the bones are covered by a thin layer of articular cartilage [1], [3]

A type of synovial joints is the hinge joint. This joint has a bone with an end convex surface that fits (articulates) into a bone with a concave surface end. This joint allows a bending and straightening motion along a single axis, which is similar to a hinge door motion. Hinge joints are functionally classified as uniaxial joint, one bone remains in a fixed position while the other moves around an axis. Examples of these joints are the elbow (Figure 5-B), ankle, knee and interphalangeal joints [1], [3].

This study is focused on the hinge joints due to the morphological and movement (uniaxial movement) characteristics which help with the simplicity's sakes in the computational model.

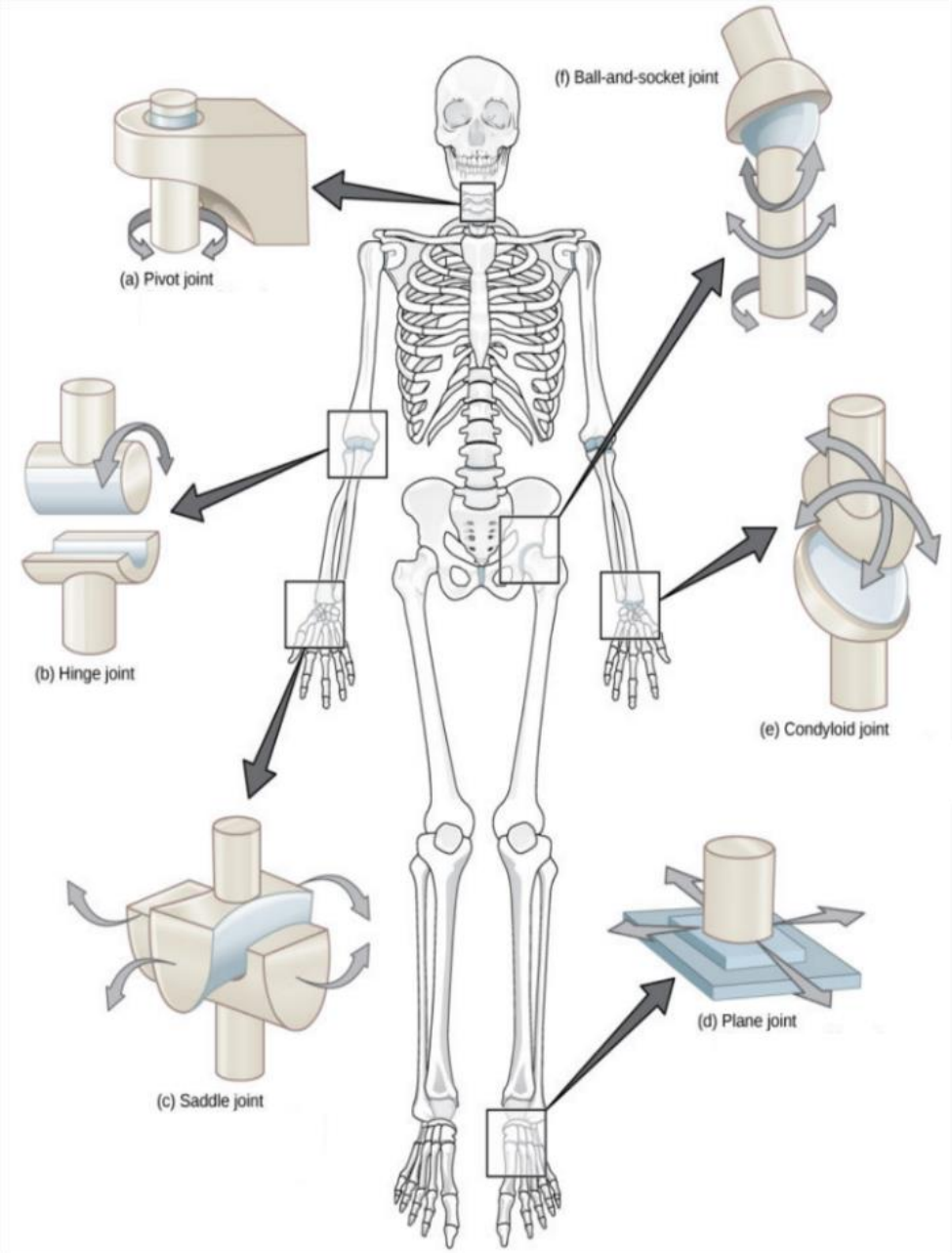

Figure 5. General types of a synovial joint in the human body. [Adapted from [1], [3]].

A) Pivot joint (between C1 and C2). B) Hinge joint (elbow). C) Saddle joint (between trapezium carpal bone and metacarpal bone). D) Plane joint (between tarsal bones). E) Condyloid joint (between the radius and carpal bone). F) Ball-and-socket joint (Hip).

3.1. Experimental works on embryo and fetal development

The first analysis of human embryo development was done in the 50's decade [11]. Ernest Gardner *et al* (1950) developed a study over 45 human embryos around the sixth and ninth week

of gestation. They analyzed different aspects of the stages of embryo development, such as the joint formation, the formation of the ossification centers, and tendon formation [11], [12]. Those experiments showed that at different stages of the embryo development the mechanical and molecular factors have influence [11], [12].

From then on, other authors as Ronan o' Rahilly *et al (1968)* proposed experimental researches that allow describing the embryonic development in terms of stages, which represent external and morphological criteria to compare the differentiation and growth. While Elemer A. (1982) described the limb bud mesenchyme interaction of particulars phenotypes structures during prenatal stages [4], [12]. Other authors as Carter *et al* (1988) identified a correlation between mechanical stimuli and the cellular behavior during fracture healing [14]. They stated that the mechanical influence can affect the cell response in different ways, for instance, the hydrostatic compression increased the specific gene expression of cartilage and cellular production [11]–[17]. In fact, they proved that different types of loads promote different types of cellular response such as skeletal morphogenesis, growth, regeneration, maintenance, and degeneration [14], [15]

From the molecular perspective, several biochemical aspects have been identified to affect the embryonic development and articular maintenance, for example, Bone morphogenetic proteins (BMP's) and the Growing and Differentiate Factors (GDF) [24], [25]. In fact, many studies have shown that after the formation of the Interzone, and the differentiation of the bone blastema into chondrocytes, the cartilage behavior is governed by a negative feedback loop involving Indian Hedgehog (Ihh) and the Parathyroid hormone-related protein (PTHrP) [26], [27]. Ihh, regulates chondrocyte maturation and hypertrophy, while PTHrP inhibits chondrocyte hypertrophy and promotes their proliferation [26]–[29].

Another biochemical variable that can be related is Hox genes. These genes are a group that specify regions of the body plan of an embryo along the head-tail axis. These genes secreted a family of proteins that encode and specify positional characteristics, which explain that these genes might regulate where the position along the chromosome corresponds at time and place of their expression over the mesenchyme during development. However, these genes were not entirely understood as well, what we know, is that Hox gene might control the differential amount and growth of tissue from proximal to distal [5], [17], [30], [31].

Additionally, to induce cell death and allow the creation of a joint space, the molecule Wnt/ β-catenin is expressed in the Interzone signalling that leads the physical separation of the rudiments [8], [32], [33] and is also observed in parts of the fibrous capsule and the synovial lining of the joint capsule [9], [34].

3.2. Computational works

Computational models of joint morphogenesis have been developed to evaluate how the joint surface moulds due to mechanical stresses. Heegaard et al. (1999), developed an interphalangeal model including muscular action (Tendons). They explore the hypothesis that mechanical stress distribution may shape the cartilage anlagen and lead to the development of congruent articular surfaces [35]. A particularity of this model is that they analyzed direct contact between the two opposite rudiments without regarding the material property (fluid condition) of the synovial capsule in the interphalangeal joint [35]. In the results was observed that during cartilage growth, the mechanical load generates a rotation over the middle phalanx that they can not explain [35].

Diversely, Giorgi et al. (2014) developed a 3D computational model of the joint morphogenesis, including the synovial joint capsule to avoid modelling the contact between each rudiment. They developed this model based on the results obtained of comparison between using direct contact between bone rudiment and the synovial joint capsule. The computational results proved no numerical difference between both models, however, the computational cost was reduced using the capsule. They obtained a proximal surface with a concave profile whereas the distal joint surface acquired a rounded convex shape for a ball and socket joint (Hip) [36]. Furthermore, they developed an interphalangeal joint considering as mechanical load a compressive load and avoiding muscular action (tendons). It was reported that both surfaces of the opposite rudiments obtained a concave shape, which is not according to an interphalangeal joint [36].

Both of the aforementioned works based on the cartilage growth and joint morphogenesis only on the hydrostatic stress distribution [35], [36]. However, the final shapes of the two opposite rudiments do not adjust entirely to a real interphalangeal joint shape. This could be an indication that biochemical interactions during bone morphogenesis might be necessary to achieve congruent joint shapes.

Based on previous works, computational and experimental, Márquez-Flórez *et al.* (2018) [9], designed a computational model to explain the interaction of these molecules that give rise to the joint onset. They included biochemical factors that may influence the Interzone onset, cell differentiation, tissue growth, cavitation process and synovial capsule development [9]. They characterize the cellular activity by a mathematical model of a reaction-diffusion system and cellular automata. This was, to our knowledge, the first study, that successfully explain how biochemical factors influence the joint development, from the bone blastema to the cavitation process, however, does not describe the morphogenesis process and the influence of mechanical stimuli.

To date, there is no experimental or computational model able to accurately explain how a synovial joint is shaped. Moreover, none of the existing models has integrated the biochemical stimulus as a factor for joint shaping. Understanding how these biochemical and mechanical stimuli influence the joint morphogenesis process might be useful for the prevention and treatment of developmental diseases.

3.3. Ossification process (Osteogenesis)

The ossification process or osteogenesis is the process of bone formation by osteoblasts [24]. It is necessary to define that ossification is a distinct process of calcification, because, he calcification occurs during the ossification of bones, and can also occur in other tissues [1], [3]. The osteogenesis process has two pathways, the first one, the intramembranous ossification, and the second one, the endochondral ossification [1], [3], [26], however, bone is the same regardless of the pathway that produced it. These process starts in the sixth or seven-week of the embryonic development when skeleton embryos consist of fibrous membranes and hyaline cartilage [1], [3].

In the intramembranous ossification, the compact and spongy bones develop directly from sheets of mesenchyme (undifferentiated) connective tissue [3], [37] (Figure 6-A). This small groups of mesenchyme cells, at his stage called a cluster of cells, starts to differentiate and change their morphology (internal structure), until they become osteoblasts [1], [3], [38] (Figure 6-B). Then, these osteoblasts create an extracellular matrix (uncalcified matrix), which calcifies (harden) a few days later as mineral salts are deposited on it, entrapping the osteoblasts within [1], [38], [39].

Afterwards, the trapped osteoblasts transform into osteocytes, while the cluster cells (osteogenic cells) in the surrounding connective tissue differentiate is still differentiating into osteoblasts [3], [39] (Figure 6-C). Some examples of bones that go through the intramembranous ossification are the skull and clavicles. The last bones to ossify via intramembranous ossification are the flat bones of the face, which reach their adult size at the end of the adolescent growth spurt [1], [3], [38], [39].

Otherwise, the other pathway of ossification is the endochondral ossification, is the process in which the bone develops replacing cartilage (Figure 6-D). This bone cartilaginous rudiment serves as templates that will be replaced completely by new bone (Figure 6-E). This ossification takes longer than the intramembranous ossification [1], [39].

Some studies identify that the Vascular endothelial growth factor (VEGF) and the TGFα are involved in the ossification process [37]. The VEGF is involved in bone angiogenesis, and in various aspects of bone development, including chondrocyte osteoblast differentiation, and osteoclast recruitment [37]. TGFα is believed to influence in early bone development, growth and

ossification [40]. During embryonic stages, TGFα regulates the endochondral ossification, the osteoclast recruitment, and the vascularization at the primary and secondary ossification centers [40], [41].

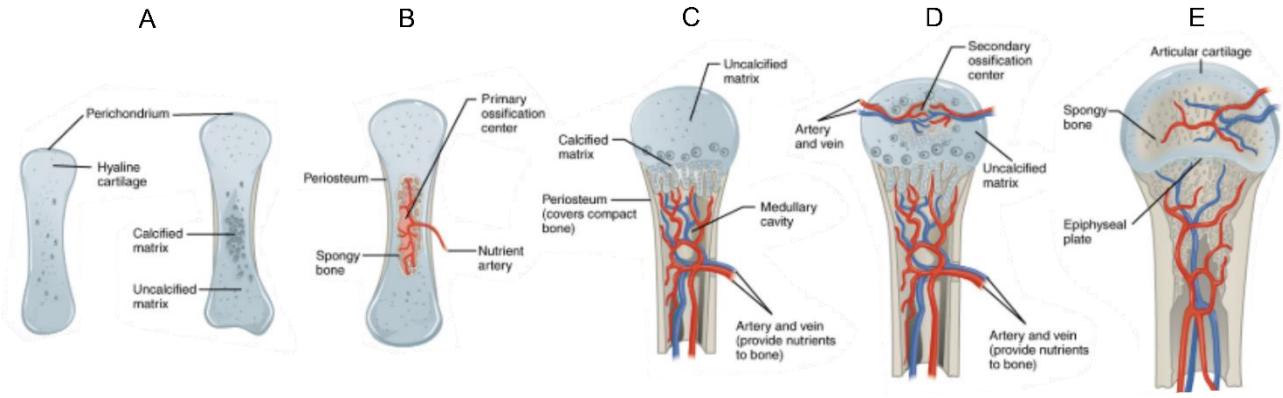

Figure 6. Osteogenesis process [Adapted from [1], [3]*].*

4. Material and Methods

In this chapter, we present the biochemical variables used a well as constants values for the computational model [9]. It was assumed that the movement, viewed at the sagittal plane, has a cyclic extension-flexion movement where the distal rudiments rotate around the proximal rudiment. For the mathematical model, all elements were considered as linear elastic materials, all the equations were solved with finite element methods as implemented in a user element Subroutine in FORTRAN and solved with ABAQUS v6.13 (Dassault Systémes USA, Waltham, MA). The domain was meshed by employing quadrilateral elements, the size of which was refined until further no longer yielded noticeable improvements. Finally, the ossification process started with the increasing young modulus of the diaphysis until it reached cancellous bone modulus (POC), while the appearance of the SOC was determined by the high concentration of osteogenic index (OI).

4.1. Biological variables

The joint development involves many molecular factors [8], some might be influenced by the VEGF is involved in bone angiogenesis, and in various aspects of bone development, including chondrocyte osteoblast differentiation, and osteoclast recruitment [37]. Furthermore, several studies have suggested a potential role of TGFα in early bone development, growth and ossification [40]. During embryonic stages, TGFα regulates the endochondral ossification, the osteoclast recruitment, and the vascularization at the primary and secondary ossification center [40]. On the other hand, exist the relationship between the Bone Morphogenetic Proteins (BMP´s) also called the Growth and Differentiation Factors (GDF´s), that, influence directly the development and maintenance of articular cartilage and join onset. However, this activation of the BMP signalling over a joint onset showed that his antagonist Noggin activates and suppresses mesenchyme cell condensation, this antagonist of the BMP family it is necessary for joint formation [7], [39].

The GDF-5 derive from the BMP family, initially stimulates cartilage formation and restrict expression of molecular markers to the appropriate location of the bone anlagen. Then induces apoptosis, however this a critical step for cavitation and joint formation, it here was the antagonist BMP (Noggin) inhibits GDF-5 expression, this with the aim of preventing cell death. The active-inhibit loop of GDF-5 and Noggin promoted interzone tissue function and preventing differentiation of mesenchyme tissue into cartilage [9], [32], [39].

Authors as Márquez-Flórez *et al*. (2018) [9], designed a computational model with the aim to explain the interaction of these molecules that give rise to the joint onset. They included the molecular factors mentioned before as the generic molecules that possibly influence the interzone onset, cell differentiation, tissue growth, cavitation process and synovial capsule development [9]. Such in that case there was considered the effect of the other molecules as PTHrP and Ihh.

These PTHrP-Ihh loop govern cartilage behaviour [26]. Ihh is said to control chondrocyte proliferation, maturation, and hypertrophy [26]–[28], [43], whereas PTHrP inhibits chondrocyte hypertrophy [27]. On the other hand, a molecule in charge of the differential growth from proximal to distal was also considered. This molecule could be related to Hox genes [5], [30], [44], or any other molecule which regulates bone growth. The HOX gene can be represented mathematically as a gradient that affects the growth rate to become from the proximal to distal promoting longitudinal growth of the limb [9]. Additionally, it was considered some remaining of the molecule Wnt (which allowed the cavitation process [8], [9], [32], [33], [45]).

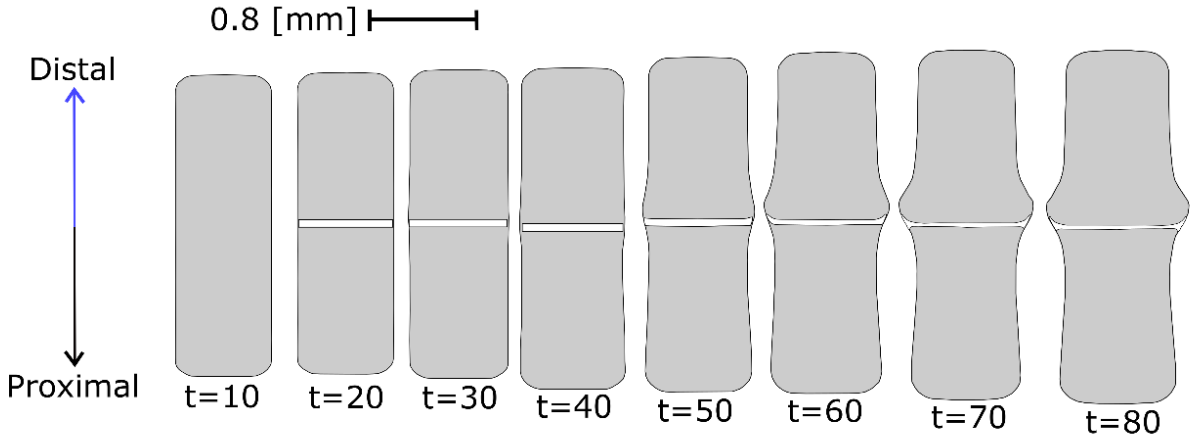

Figure 7. Process of the joint onset development.

A different time step of the biochemical computational model[9], Final geometry took from the last time step t=80

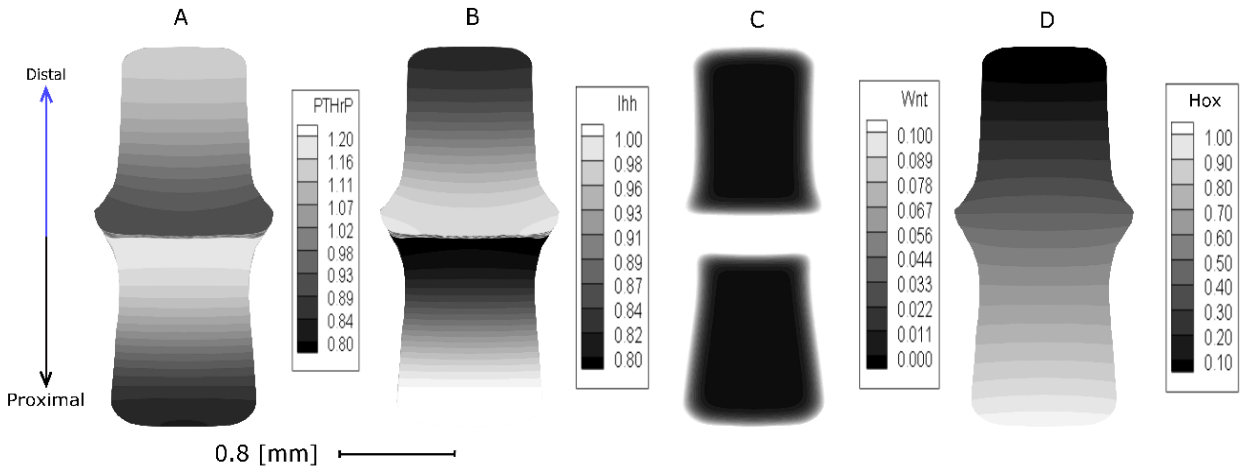

Figure 8. Results of the biochemical distribution over the two opposite rudiments in the last time step of the model [9].

A) PTHrP. B) Ihh. C) Wnt. D) Hox[9]

The initial concentrations of the aforementioned molecules were taken from the last step of a former study of our research group [9]. For the molecular concentration changes, the bone anlagen were divided into areas proportional to their lengths, while the concentration of the molecules was kept constants within each corresponding area for each time step (Figure 8).

Table 1. Maximum and minimum values of the molecular parameters included in the mechanobiological model [9]

Parameter	Min Value	Max Value
PTHrP	0.80	1.20
Ihh	0.80	1.00
Hox	0.00	1.00
Wnt	0.000	0.100

4.2. A mathematical model with the Finite Element Method (FEM)

4.2.1. Boundary conditions

The geometry of the model was approximated and adapted from the last step of a former study of our research group [9]. For the flexion-extension movement, we used only four steps of the movement were evaluated, the distal rudiment was at 90º, 60º, 30º and 0º with respect to the vertical line *y* (Figure 9).

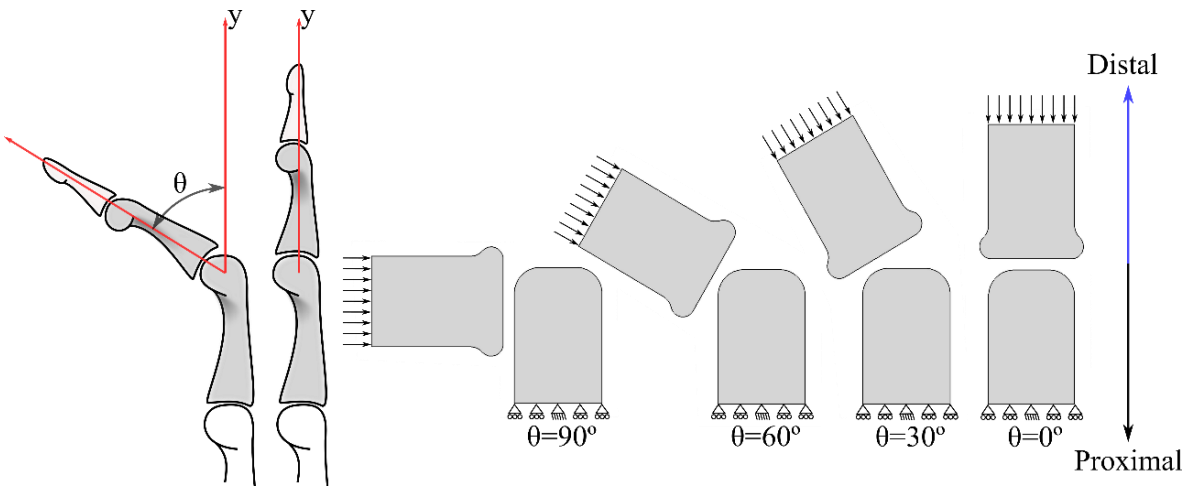

Figure 9. Boundary condition implemented on the model [Authors].

The inferior boundary of the proximal rudiment has a central node fixed, other nodes allow lateral displacement. [Authors]

Regarding the mechanical part of the model, an axial displacement of 1μm was applied on the upper boundary of the distal phalanx at each motion stage (Figure 9). The displacement had distal to proximal direction related to the opposite rudiments (Figure 9). The proximal rudiment was fixed on its bottom central node, the other nodes of the bottom end could move on the lateral direction. For simplicity's sake, some considerations were made, *i.e*. the modelling of contact between the phalanges was avoided by including the synovial capsule, also, all tissues were modelled as linear-elastic, isotropic and homogeneous materials. The cartilage of the anlage bones and the synovial capsule was assumed as totally incompressible (Poisson ratio of 0.49). Each cartilage rudiment section had a young modulus of 1000 kPa, while the synovial capsule had a young modulus of 1 kPa, establishing a relation 1000:1 between them.

$$\int_{\Gamma} \underline{\underline{N}}^{T} \cdot \underline{T}\, \partial\Gamma \qquad \text{Eq. 1}$$

This equation represents the boundary conditions implemented on the mathematical model, the commercial software solves internally by the penalty method. In that case, does not need to programme the method on a subroutine. The model identifies the boundary (connection element and nodes) and takes it into account solving the differential equation element by element.

4.2.2. Translated and rotated elements

After obtained the results of stresses on each phase of motion (90°, 60°, 30° and 0°), we overlap the stresses on a reference position (0°). It was computed the average stress for each element. It was calculated the centroid of the elements in each rudiment in all phases of motion (90°, 60°, 30° and 0°) including the reference position (0°). These centroids were mapped (translated and

rotated) over the reference position (0°) and overlapping the computed centroids of the compared geometries. Subsequently, the computed centroids of the reference position took the closest point of the mapped centroid of the element. The points that did not have an element close to them were discarded. These centroids points contain the value of the octahedral, hydrostatic and shear stress obtaining in each phase of motion (0°, 30°, 60° and 90°).

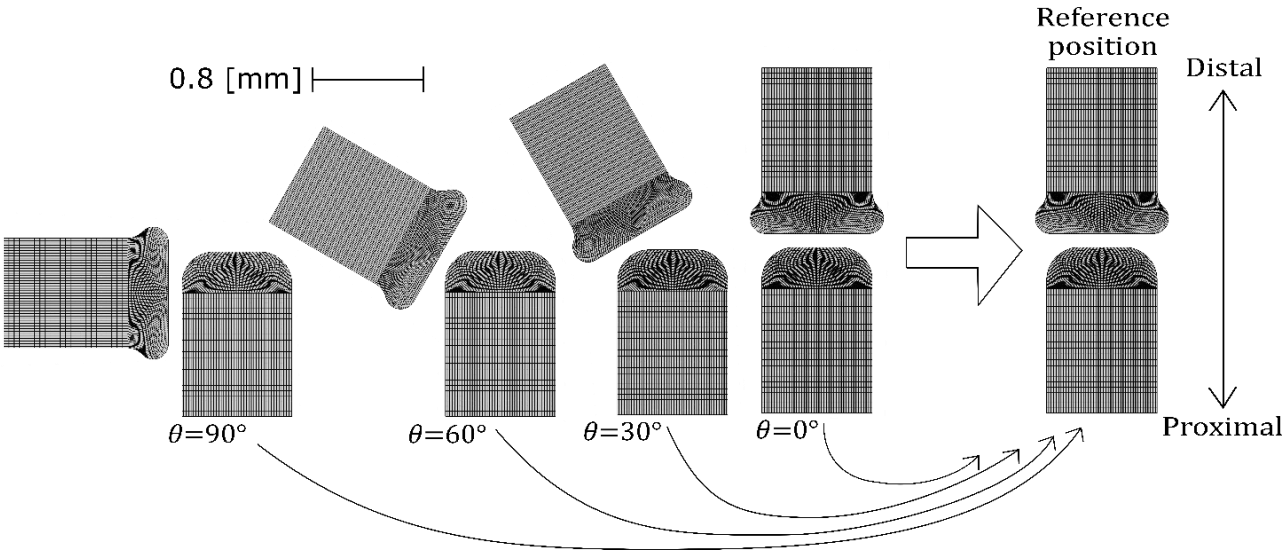

Figure 10. Translation and rotation of the centroid elements of each rudiment [Authors].

The flexion-extension movement from 90° to 0° to the reference mapping position. [Authors]

After the stresses were moved and rotated, it was calculated an average value on the reference position of octahedral, hydrostatic and shear stress. The average stress was calculated as the sum of the stresses of each element of the rudiment in the reference position and divided by the number of flexion-extension movements (0°, 30°, 60°, 90°) uses during the model (4).

$$\hat{\sigma} = \sum \frac{\sigma_{0°} + \sigma_{30°} + \sigma_{60°} + \sigma_{90°}}{4} \qquad \text{Eq. 2}$$

We presented in Eq. 2 the average equation uses for the average octahedral shear, hydrostatic and shear stress (Figure 13).

4.2.3. Biological growth

For the cellular aspect, we considered that in joint morphogenesis the cartilage growth has a relationship with mechanical stimuli and the molecular interactions, their response to mechanical stimuli was included as a positive relationship between cyclic hydrostatic stress and the cartilage growth [46]. Additionally, it was considered that high concentrations of PTHrP and Wnt promote chondrocyte proliferation, therefore, cartilage growth. Hence, if a cartilage element had PTHrP

and Wnt concentrations above a threshold (TH_{PTHrP} as 1.1 and TH_{Wnt} as 0.01), the element's strain tensor (d^{growth}) was defined as in Eq. 3, else, as zero

$$d^{growth} = \alpha S_{Hyd} \delta_{ij} \boldsymbol{e_i} \otimes \boldsymbol{e_j} \quad \text{Eq. 3}$$

S_{Hyd} is the hydrostatic stress of the element; α, is a constant that indicates the influence of the Hydrostatic stress on the element's isometric growth, has a value of two (2.0) or zero (0), $\mathbf{e_k}$ are the unitary directional vector in a Cartesian coordinate system; δ_{ij} is the Delta-Kronecker tensor; and i, j take values of 1 or 2 (*x*-direction and *y*-direction). In the growth equation, the hydrostatic stress S_{Hyd} had a volumetric effect by increasing cell quantity, without increasing cell concentration [cell/unit volume].

4.3. Modelled cases

The model was tested in seven different cases (Table 2). The first one replicates normal conditions and the following four simulated pathological settings. In the first pathological setting, the effect of the molecules was not considered; the growth depended only on the hydrostatic and octahedral stresses. In the second one, a dislocation of 0.3 μm between the two phalanges was included (Figure 11). Moreover, four palsy environments were simulated in which the only one rotated position was considered; the distal phalanx was at 0º or 90º flexion angle with and without (w/o) molecular effect.

Table 2. Conditions of normal and pathological cases modelled [Authors]

		Angles (Degrees)	Molecular effect	Mechanical effect	Average Stresses	Dislocation
Normal		90° 60° 30° 0°	Yes	Yes	Yes	0 μm
Pathological	**w/o molecular**	90° 60° 30° 0°	No	Yes	Yes	0 μm
	Kilter	90° 60° 30° 0°	Yes	Yes	Yes	0.3 μm
	0° Palsy	0°	Yes	Yes	No	0 μm
	0° Palsy	0°	No	Yes	No	0 μm
	90° Palsy	90°	Yes	Yes	No	0 μm
	90° Palsy	90°	No	Yes	No	0 μm

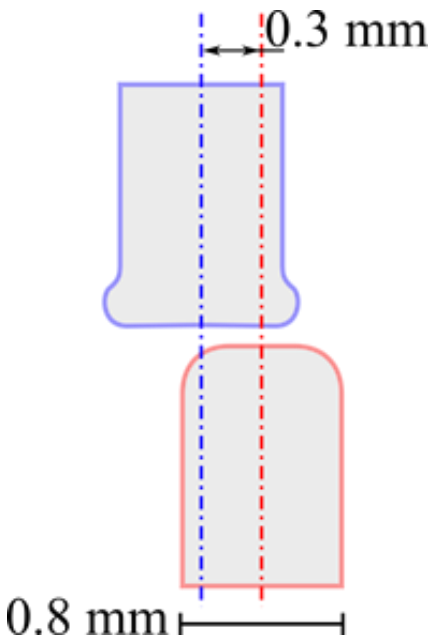

Figure 11. The geometry of the pathological kilter model [Authors].

Distal phalanx in blue and the proximal phalanx in red. The palmar side is on the left and dorsal side at the right [Authors]

4.4. Ossification Process

During the embryonic development large bones develop as process known as endochondral ossification, the ossification starts with the hypertrophy of chondrocyte that is located on the central zone of the bone rudiment (diaphysis), were the hypertrophy chondrocyte promotes calcification of tissue and the recruitment of mature woven bone as osteoblast and osteoclast [47], [48]. Although the Primary Ossification Centre (POC) origins on the diaphysis, subsequently, the adjacent chondrocyte in hypertrophy zone obtaining a flattening morphology and columnar organization along the growth direction [47]–[49]. In prenatal stages, the extreme section of the bones (epiphysis) proximal and distal heads exist cartilaginous tissues, in these areas appear the Secondary Ossification Centers (SOC) [50].

The responsible the structure growing is known as the growth plate, this was located between the ossify tissue POC and SOC [49], [50]. Histologically the growth plate were organized in three types of structure, the first, it is known as reserve zone, a similar structure as the articular cartilage, further, becomes the proliferative zone, here the chondrocyte has a flattened structure and columnar organization, and the last one, was constitutive by hypertrophy chondrocyte, furthermore, this chondrocyte starts the apoptosis and the matrix calcified. [47]–[49]. However, Carter et al (1988, 2003) [15], [51] define another parameter to identify zones of cartilage next to ossify called the Osteogenic Index (OI).

The OI is a scalar parameter which considers the effect of the hydrostatic stress and the octahedral shear stress [49]. This parameter, OI, can be used to predict which regions of the cartilaginous anlage are likely to ossify first (high OI) [15]. The osteogenic index (OI) was calculated and used to predict the appearance of the POC and SOC within the anlage [41], [48], [51]. Therefore, the cartilage on the diaphysis was considered to ossify under high OI (Eq. 4) and low PTHrP and Wnt, whereas for the SOC, only the OI was considered.

$$OI = K_1 S_{Hyd} + K_2 S_{Oct} \quad \text{Eq. 4}$$

S_{Hyd} is the hydrostatic stress; S_{Oct} is the octahedral shear stress; k_1 and k_2 are the constants weighting the contribution of S_{Hyd} and S_{Oct}, respectively. k_1 took the value of 0.7 and k_2 of 1 for the proximal phalanx and the -0.35 and 1, respectively, for the distal phalanx. The ossified tissue of the POC was modelled by increasing the element's young modulus until it reached 20000 kPa.

Finally, we describe the computational model procedure in a flowchart, it includes brief ideas of material and methods and a criterion for stopping the simulation process.

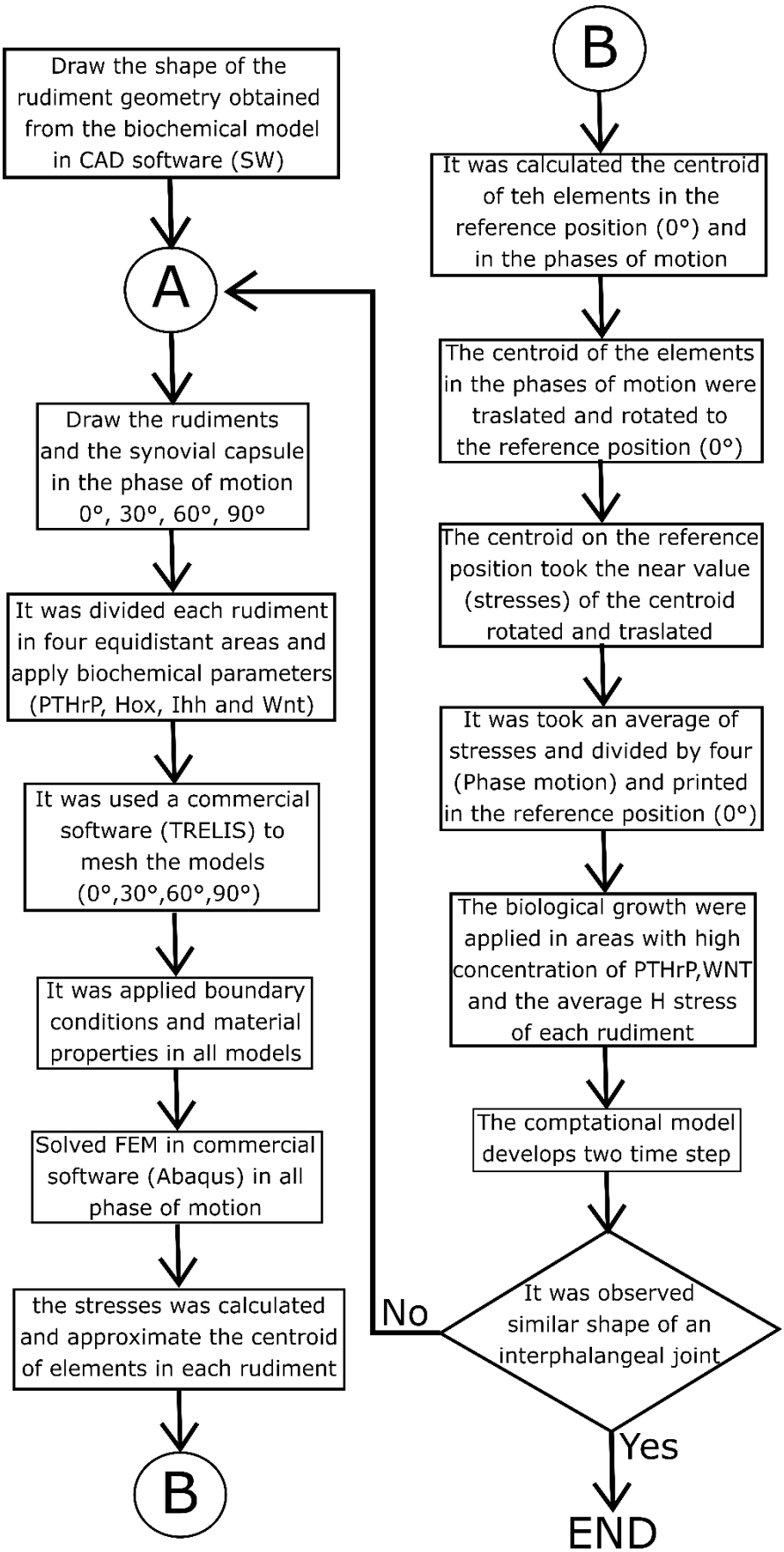
Draw the shape of the rudiment geometry obtained from the biochemical model in CAD software (SW)
A
Draw the rudiments and the synovial capsule in the phase of motion 0°, 30°, 60°, 90°
It was divided each rudiment in four equidistant areas and apply biochemical parameters (PTHrP, Hox, Ihh and Wnt)
It was used a commercial software (TRELIS) to mesh the models (0°,30°,60°,90°)
It was applied boundary conditions and material properties in all models
Solved FEM in commercial software (Abaqus) in all phase of motion
the stresses was calculated and approximate the centroid of elements in each rudiment
B
B
It was calculated the centroid of teh elements in the reference position (0°) and in the phases of motion
The centroid of the elements in the phases of motion were traslated and rotated to the reference position (0°)
The centroid on the reference position took the near value (stresses) of the centroid rotated and traslated
It was took an average of stresses and divided by four (Phase motion) and printed in the reference position (0°)
The biological growth were applied in areas with high concentration of PTHrP,WNT and the average H stress of each rudiment
The comptational model develops two time step
It was observed similar shape of an interphalangeal joint
No
Yes
END

5. Results

In this chapter, we presented the results of the joint morphogenesis for a normal joint development and some pathological cases which no existing relationship between mechanical and molecular, the average stress distribution over the two opposite rudiments (normal and pathological), the interaction of the molecules during the anlagen growth as PTHrP, Ihh, Hox and Wnt in different time steps of the model, and the computer analysis of the secondary ossification centers. The secondary ossification centers were computed by the osteogenic index (OI), which interacts with the stresses on the epiphysis of each rudiment, the diaphysis was considered completely ossified and the growth plate was not taken into account.

5.1. Normal joint morphogenesis model

An average result was calculated considering each finger flexion angle and translated to a reference position (0º flexion angle); all the finger positions were given the same weight. The results show the morphogenesis process of a phalangeal joint (Figure 12). The upper surface of the proximal bone molds into a concave shape, whereas the bottom surface of the distal phalanx sculpts into a convex form. The obtained shape of the joint was similar to that of an interphalangeal joint observed in the sagittal plane (Figure 12)

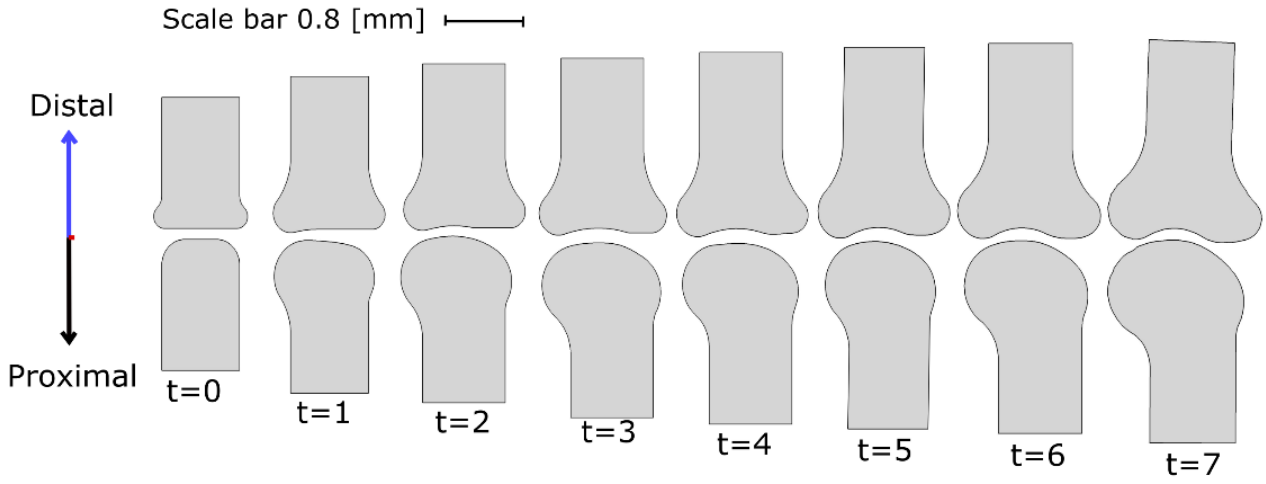

Figure 12. Morphogenesis of interphalangeal joint [Authors]

On the other hand, the octahedral shear, the hydrostatic and the shear stress distribution were obtained for different time steps (Figure 13). The proximal phalanx had high compressive hydrostatic stress on the anterior part of the joint surface, the main zone in contact with the distal rudiment (Figure 13). As for the distal rudiment, it also had high compressive hydrostatic stress

on its anterior side, but along the whole anlage, especially for the first steps (Figure 13). On the last steps, the hydrostatic stress distribution remains almost the same for the proximal anlage. However, for the distal one, it tends to become more uniform on the bone diaphysis (Figure 13). Also, hydrostatic compressive stress on the head of the distal bone is smaller compared to the rest of the bone (Figure 13).

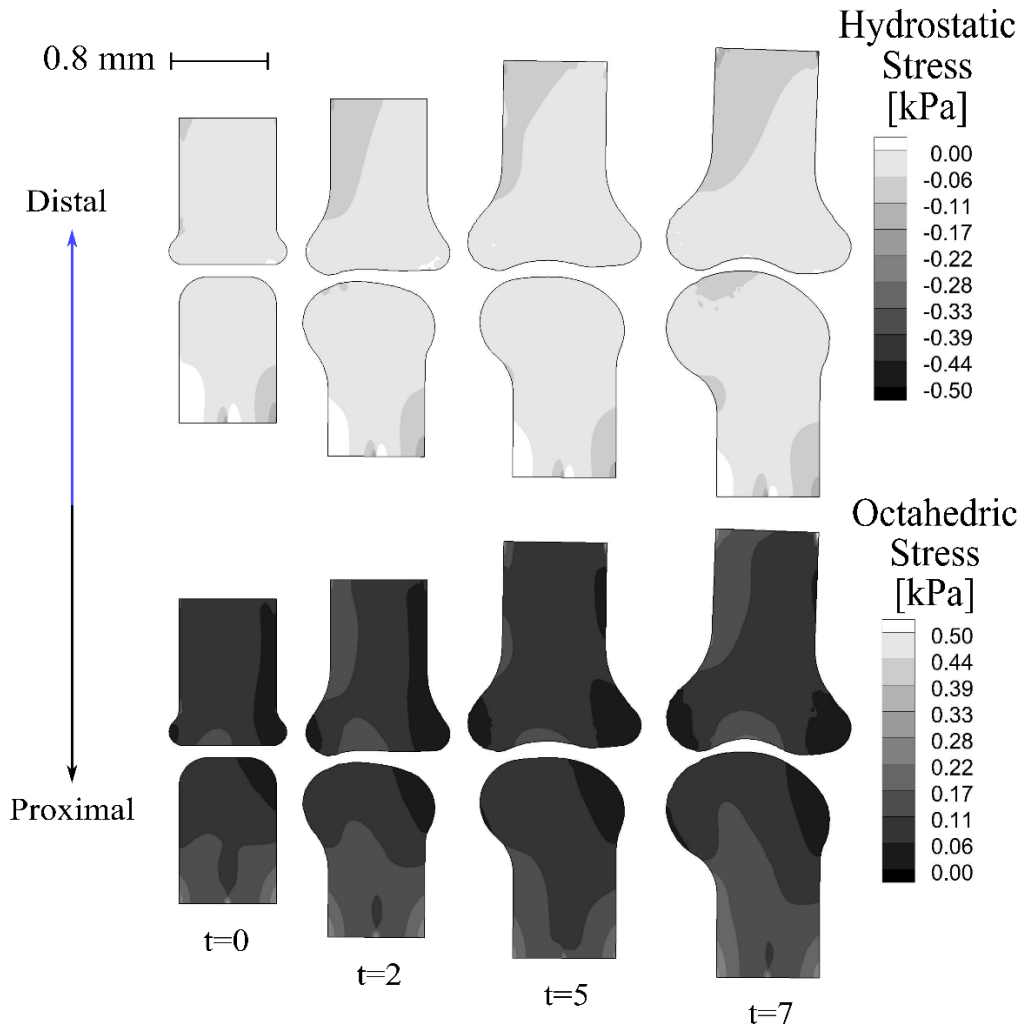

Figure 13. Stress distribution of the computational model at different time steps [Authors]

The molecular distributions were also calculated (Figure 14). PTHrP had a high concentration on the top part of both phalanges, distal and proximal (Figure 14-a). Conversely, Ihh concentration was high on the bottom part for both phalanges (Figure 14-b). On the other hand, Wnt was higher on the head of both phalanges (Figure 14-c), whereas the Hox molecules had a gradient from proximal to the distal direction (Figure 14-d).

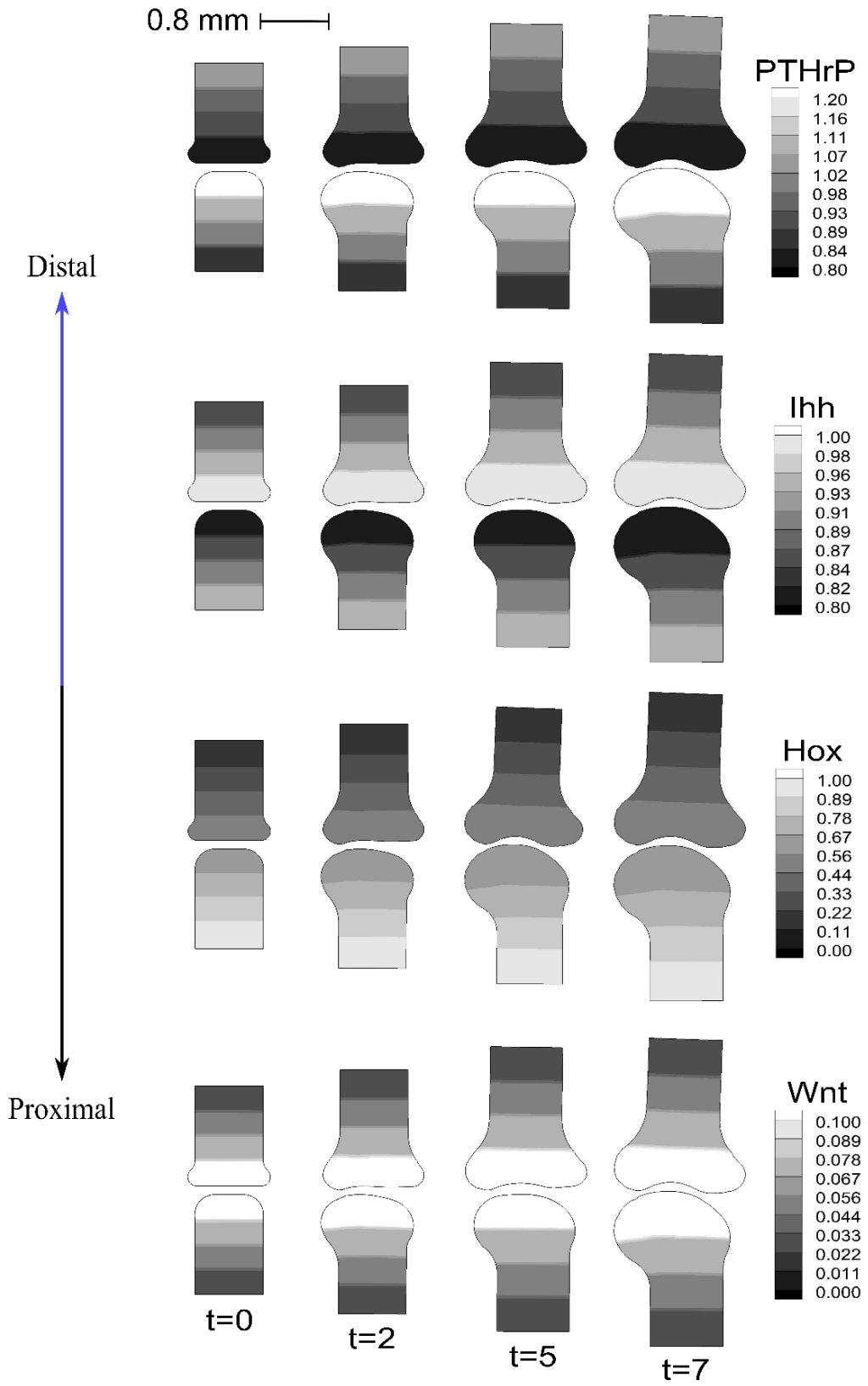

Figure 14. Molecular distribution for the joint morphogenesis. [Authors]

The different time step of the molecular distribution for normal conditions. PTHrP, Ihh, Hox and Wnt. The palmar side is at the left and the dorsal side at the right [Authors].

5.2. Pathological joint morphogenesis models

It was considered some pathological environments that were simulated to evaluate some conditions that might be present during development which can affect the joint morphogenesis (Figure 15). The first one tested the conditions when the molecular effect is neglected which produced and abnormal growth of the rudiments. The distal one grew much more than in normal conditions and there was the absence of the head structure of the bone anlagen, while in the proximal rudiment the head developed in an abnormal shape.

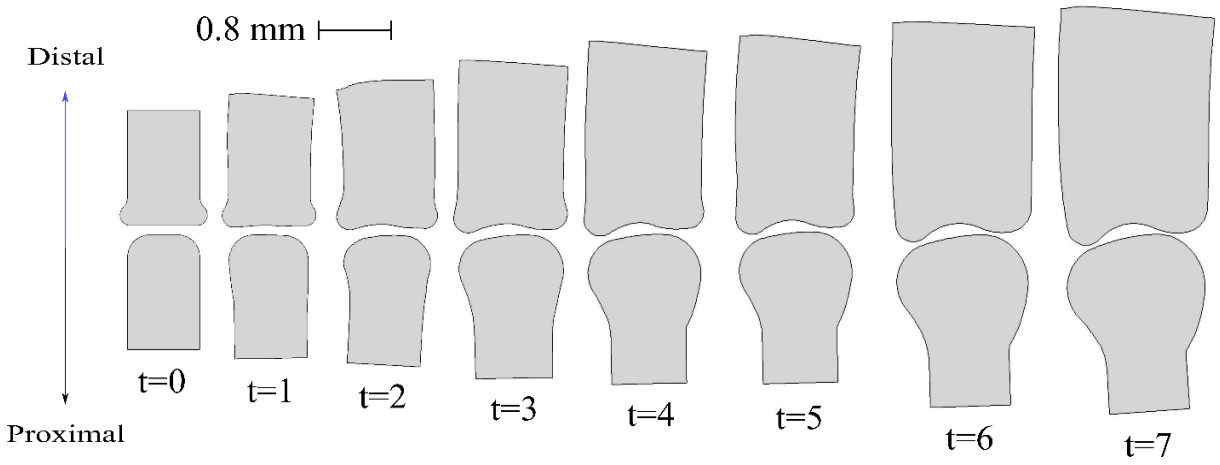

Figure 15. Results of the first case of the pathological model. [Authors]

Pathological model without molecular interaction in all-time steps [Authors].

It was observed that the hydrostatic and octahedral stress distributions were similar to normal conditions (Figure 16); the proximal phalanx had high compressive hydrostatic stress on the palmar and top part of the rudiment surface, whereas the distal rudiment had high compressive hydrostatic stress on its palmar side, but along the length of the anlage. As for the octahedral stress distribution, it was a high ant the bottom of the proximal rudiment and in the contact surface of the distal, like in normal conditions.

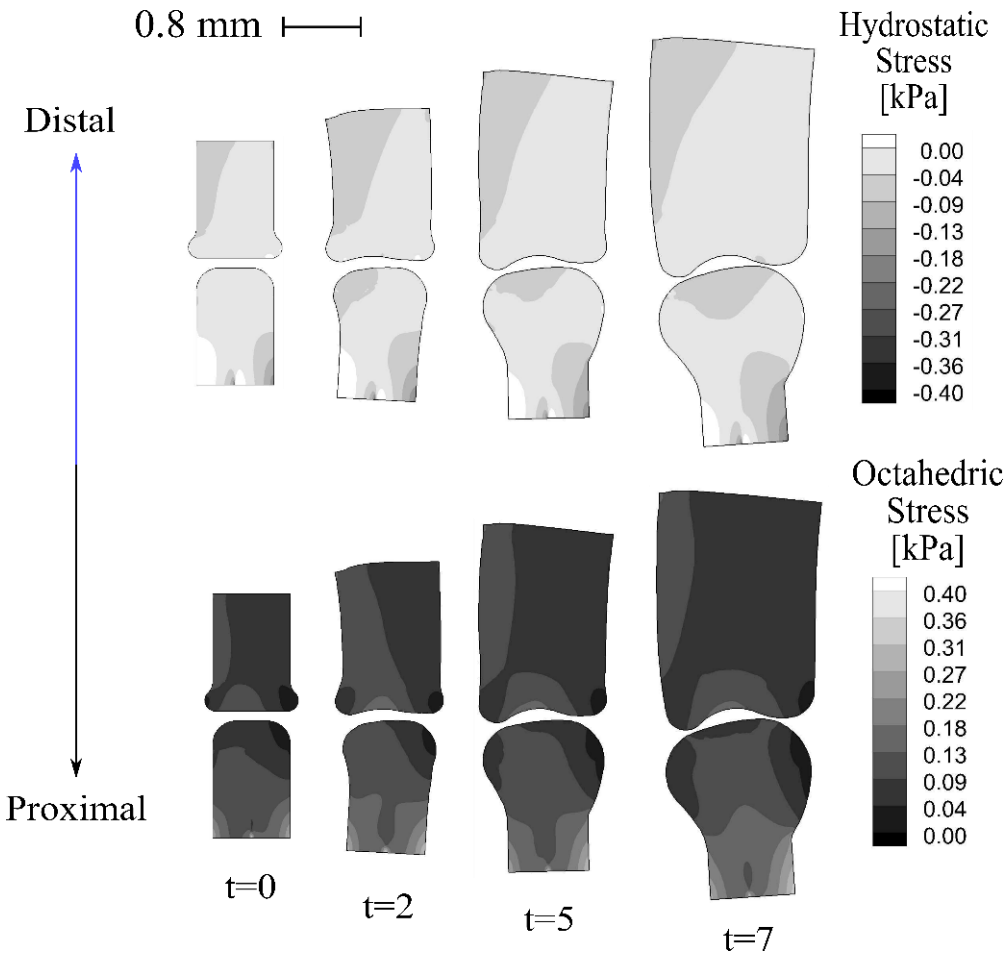

Figure 16. Mechanical stress distribution in the first pathological case. [Authors]

Pathological model without molecular interactions in different time steps [Authors]

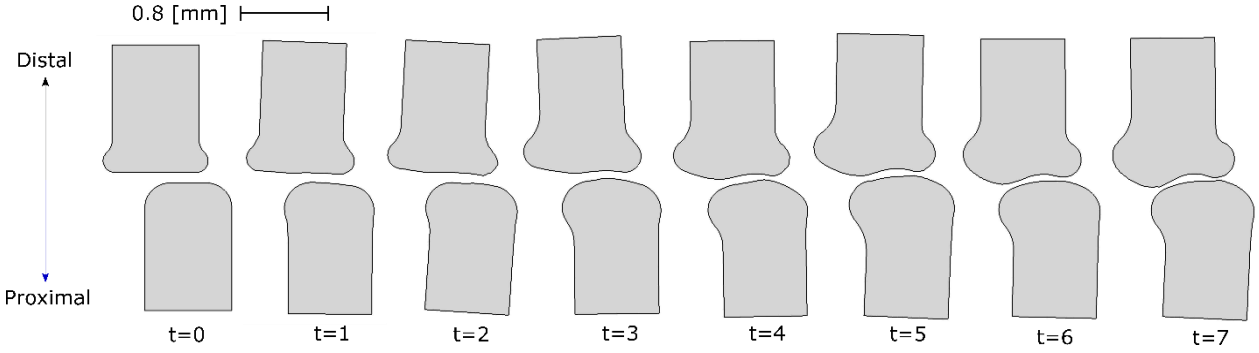

Figure 17. Joint morphogenesis of the second pathological case. [Authors]

Kilter model considered mechanical and molecular interaction in all time steps. The palmar side on the left and the dorsal side to the right [Authors].

The second pathological setting (Kilter) tested the conditions when there was an offset; the distal phalanx was moved 0.3 *mm* to the palmar side. For the kilter model, all the positions (90º, 60º, 30º and 0º) were considered to influence the joint morphogenesis. In the end, an abnormal form of the joint was obtained in which the distal phalanx appears to have the concave shape on its

dorsal side, while the proximal phalanx is shaped like a concave geometry, similar to that of normal conditions (Figure 17).

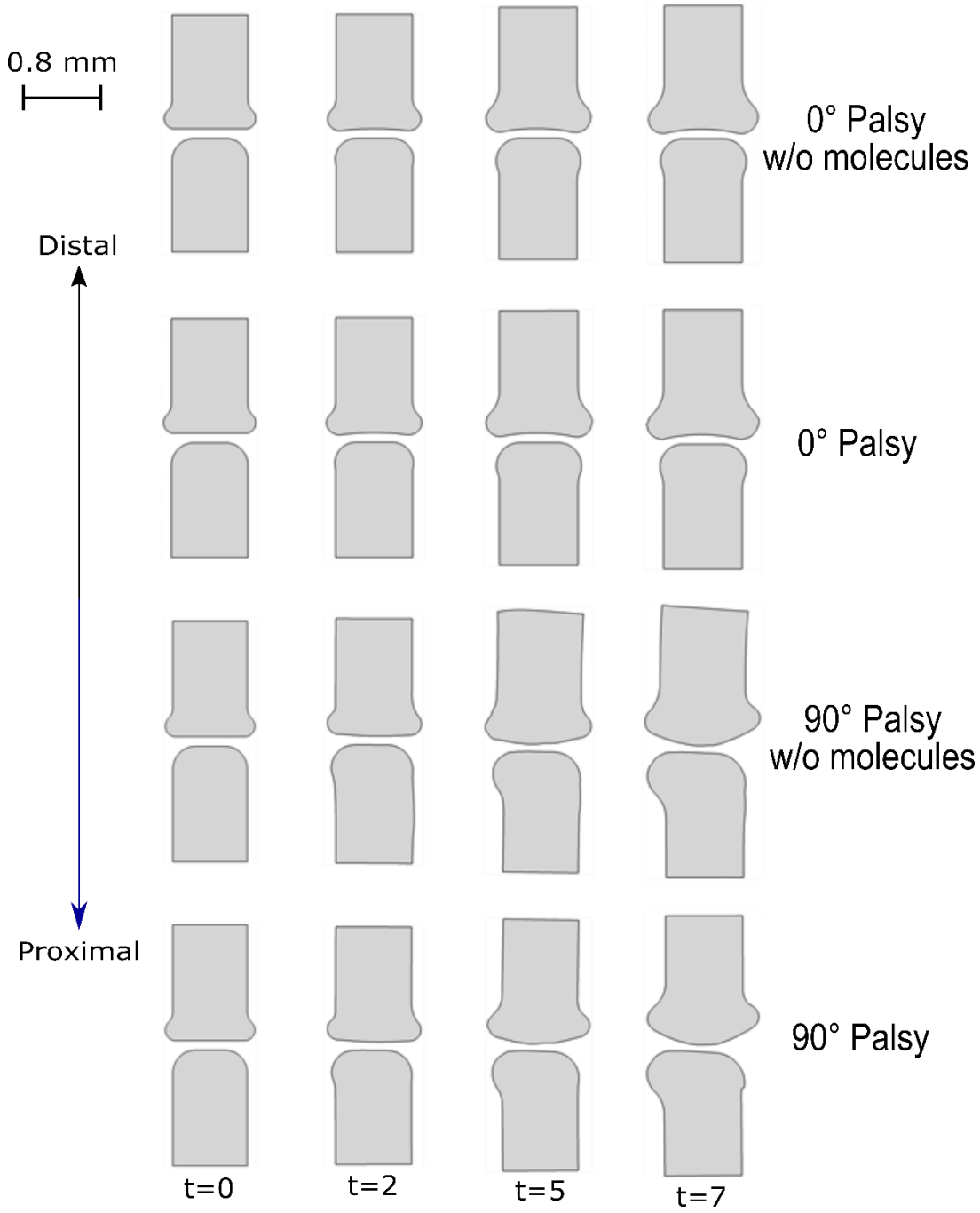

Figure 18. Results of the pathological joint morphogenesis models [Authors]

The pathological model of 0° and 90° with and without molecular effect in different time steps. The palmar side is at the left and the dorsal side at the right [Authors].

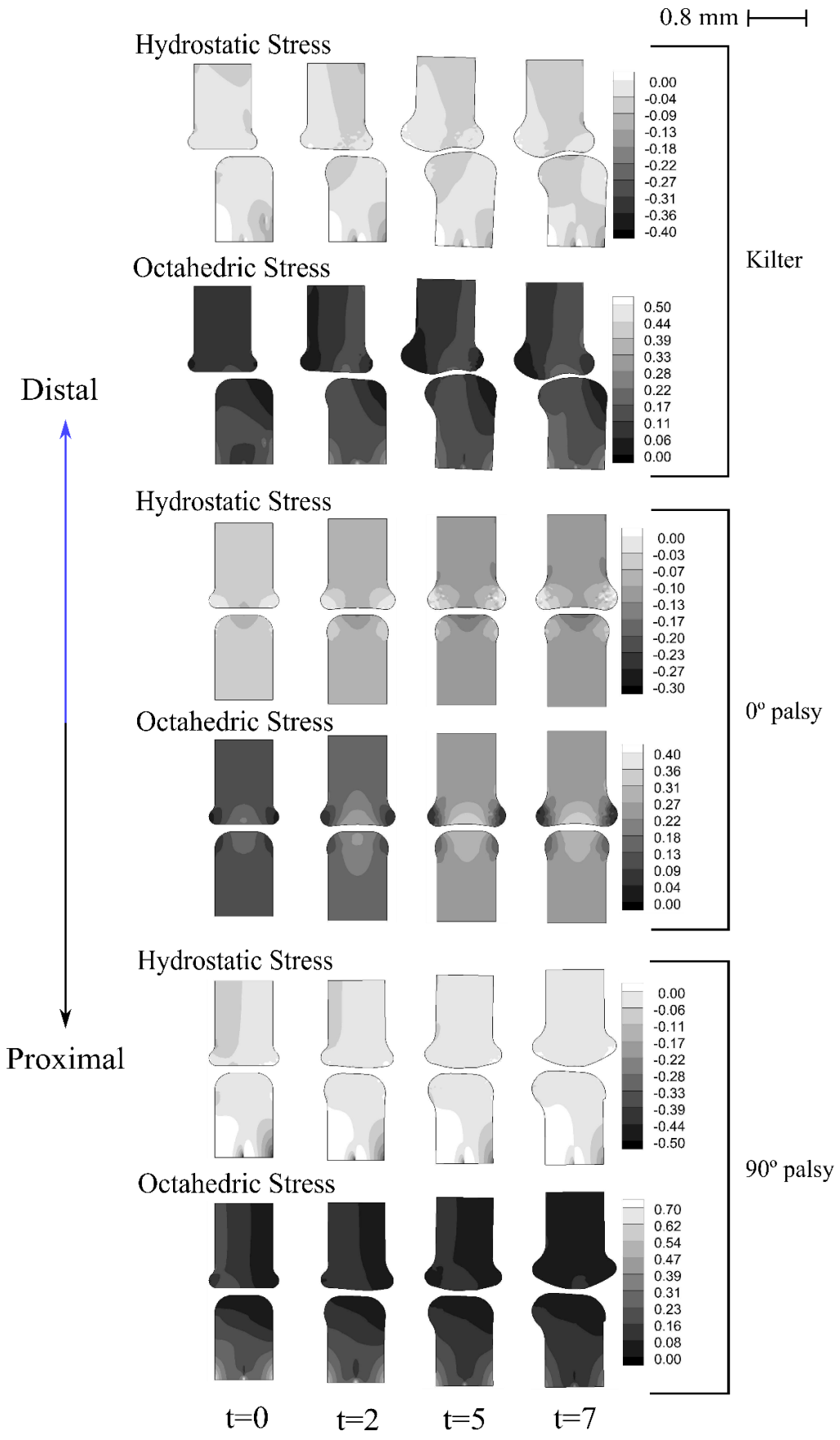
0.8 mm
Hydrostatic Stress
0.00
-0.04
-0.09
-0.13
-0.18
-0.22
-0.27
-0.31
-0.36
-0.40
Octahedric Stress
0.50
0.44
0.39
0.33
0.28
0.22
0.17
0.11
0.06
0.00
Kilter
Distal
Hydrostatic Stress
0.00
-0.03
-0.07
-0.10
-0.13
-0.17
-0.20
-0.23
-0.27
-0.30
Octahedric Stress
0.40
0.36
0.31
0.27
0.22
0.18
0.13
0.09
0.04
0.00
0º palsy
Hydrostatic Stress
0.00
-0.06
-0.11
-0.17
-0.22
-0.28
-0.33
-0.39
-0.44
-0.50
Octahedric Stress
0.70
0.62
0.54
0.47
0.39
0.31
0.23
0.16
0.08
0.00
90º palsy
Proximal
t=0
t=2
t=5
t=7

Figure 19. Mechanical stress distribution in the pathological models [Authors]

Pathological joint morphogenesis models in different time steps. The palmar side is on the left side and the dorsal side at the right [Authors]

Additionally, four paralysis environments were tested in which the phalanges were kept at a fixed angle throughout the simulation, 0º and 90º palsy were modelled for each angle, the effect of the absence of the molecules was also evaluated. Undoubtedly, the paralysis environment affects the joint shape, since no coherent joint shape was obtained in neither case of paralysis (Figure 15). For the 90º palsy model, on both w/ and w/o molecular effect, the distal phalanx did not obtain a convex shape, while for the 0º palsy model the distal phalanx had a shallow convex shape.

The joint shape is affected due to the changes in the hydrostatic and octahedral stresses distribution (Figure 16). In the kilter model, the stress distribution within the proximal phalanx was similar to the one in normal conditions, however, for the distal phalanx the hydrostatic stress was not as high in the palmar side as in normal conditions, and the octahedral stress had high concentrations at the zone of contact.

In the paralysis models, at 0º, the hydrostatic and octahedral stresses for both phalanges were mostly concentrated at the center of the geometries at all time-steps. Whereas for the 90º palsy models the hydrostatic stress was almost uniform for the distal phalanx, and the proximal had higher hydrostatic compression stress at the dorsal side. As for the octahedral stress of the 90º palsy, it banded in a similar way of normal conditions for both, distal and proximal phalanx. However, the distal phalanx did not have a zone of high concentration of octahedral stress at the contact surface (Figure 19).

5.3. Endochondral Ossification

During the endochondral ossification described that the diaphysis structure becomes the hypertrophy chondrocyte that makes apoptosis and this matrix calcified totally, such in this case, the young modulus increased in the respective area of the diaphysis until obtain young modulus of cancellous bone. The OI was observed future zones of the epiphysis and within the proximal and distal heads that can ossify (Figure 20).

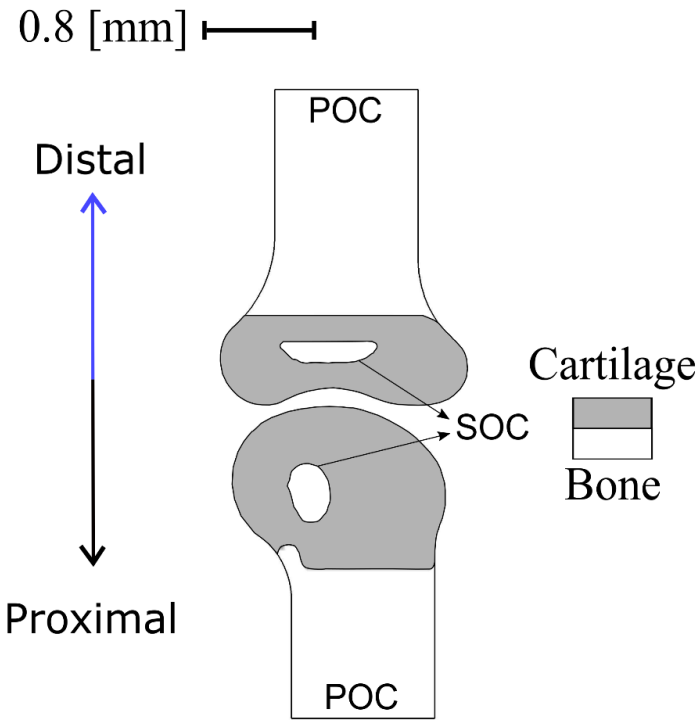

Figure 20. Representation of the POC and SOC by the OI [Authors]

Results of the OI representing the Primary and Secondary Ossification Centers (POC and SOC) [Authors]

The OI concentration was variable depending on each rudiment, the proximal sediment response to the octahedral stress and the distal rudiment to the shear stress (Figure 20). We can observe with the white color the ossified section of rudiment, and with the grey color, we distinguish the cartilage area on the heads and the appearance of the SOC is within the epiphysis if the rudiments.

6. Discussion

Previous works have tried to describe the joint morphogenesis as a result of how the cartilage tissue responds to hydrostatic stress distribution [35], [36]. These works showed how both ends of the opposite cartilage changed their shape according to the hydrostatic stress distribution, however, the obtained final shapes of the two opposite rudiments do not adjust entirely to a real joint shape.

Therefore, it is possible that not only the mechanical environment affects the morphogenesis of the heads of the bones, but also there are molecular aspects that should be considered. A former study has analyzed the joint onset from the appearance of the interzone to the cavitation process [9]. During these stages, the interaction of molecules is the ones that regulate the joint development process [9].

In this study, we are assuming that the joint movement was defined in four different positions of the interphalangeal joint. The stresses values obtained at each position were rotated and translated to a reference position (0º flexion-extension movement) and calculated an average value of stresses. The same weight was given to each position, however, there are no reports in the literature about how the finger movements during the embryo development in the morphogenesis stage are.

Nevertheless, it was considered that hydrostatic stress and the molecular concentrations of PTHrP, Ihh, Wnt and Hox were considered to play a role during joint morphogenesis. The results obtained with the model are coherent with those seen in the literature (Figure 21).

The appearances of SOC y POC were also simulated (Figure 23). SOC emerged on the top head of the proximal phalanx and on the bottom head of the distal phalanx (Figure 23).On the proximal phalanx, it was formed as a circular-shaped structure, which probably also helped mould the articular surface of this phalanx with a concave shape. On the distal anlage, the SOC took an elliptical shape, most likely due to how the convex surface distributed the octahedral shear stress and hydrostatic stresses (OI) (Figure 23).

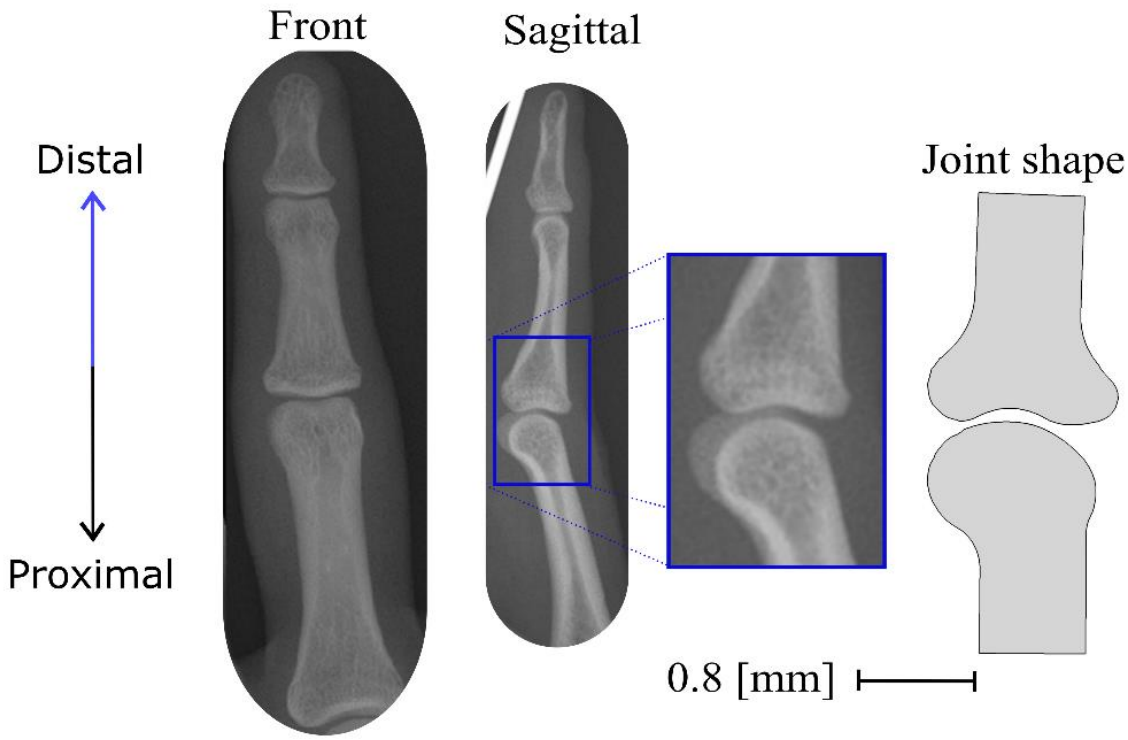

Figure 21. Comparison with an x-ray phalanx and the result from the joint morphogenesis computational model [Authors]

When pathological conditions were simulated it affected the joint development, resulting in an abnormal geometry for all cases (Figure 22). In the pathological setting where the effect of the molecules was retired from the model, the obtained geometry was much larger than normal conditions, this abnormal growth might be since the effect of the stresses is not limited by the molecular concentrations. In the pathological setting where the phalanges were dislocated (kilter) the hydrostatic stress was almost similar for the proximal phalanx, but for the distal, it had lower values than in normal conditions. Also, the octahedral stress was higher than in normal conditions, which in combination with the lower hydrostatic stress provoked a lower overall growth (Figure 19).

As for when the finger was kept straight (0º palsy), the hydrostatic stress and the octahedral stress were higher than in normal conditions, which also influenced on the overall growth of the phalanges (Figure 22). Moreover, when the paralysis model was kept with a 90º flexion, the hydrostatic stress was smaller than in normal conditions, as well as the octahedral stress; in fact, for the distal phalanx there was no zone of high octahedral stress, therefore, nothing inhibited the cartilage to grow which resulted in the absence of the convex shape in the distal phalanx articular surface (Figure 22).

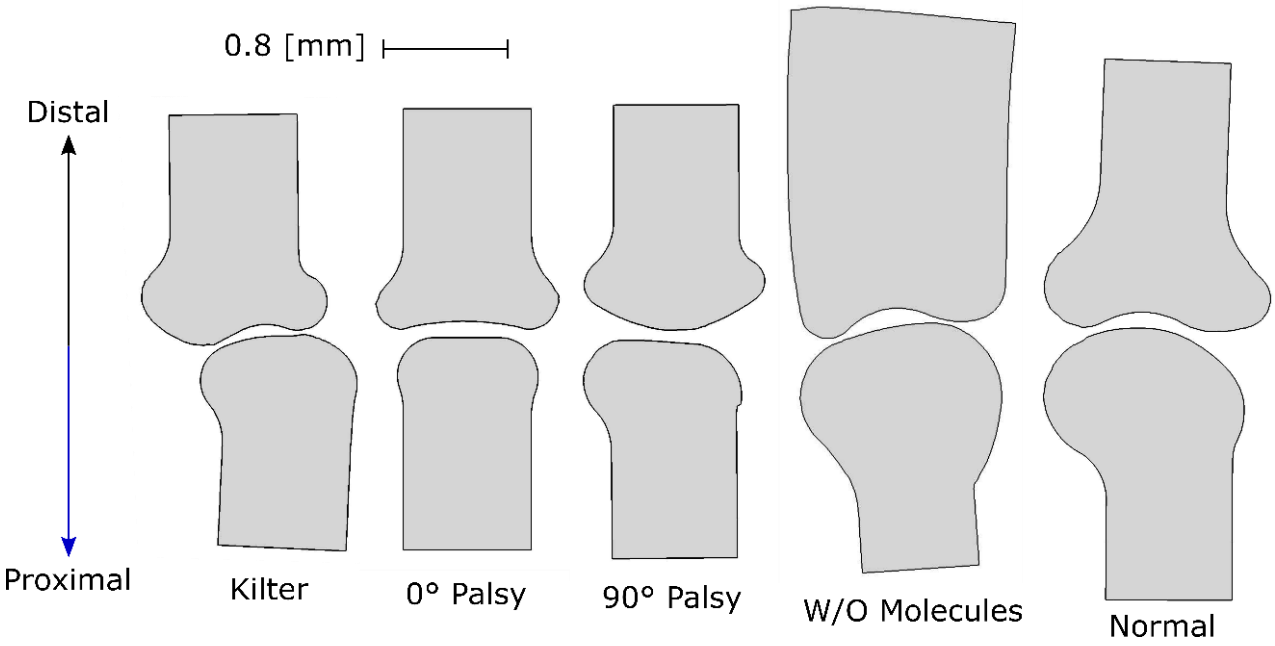

Figure 22. Total comparison between normal and pathological models [Authors]

The PTHrP-Ihh self-regulatory loop (activator-substrate) is known for its influence on long bone ossification processes [39]. The role of PTHrP is to maintain the proliferative state of the chondrocytes on the diaphysis of bones, where it has high concentrations. On the places of low concentrations of PTHrP (where Ihh is highly concentrated), the chondrocytes hypertrophy, and eventually, the tissue ossifies forming the POC.

Moreover, as part of the endochondral ossification, the effect of the OI is included, the onset of SOC within the proximal and distal heads can be also explained, as we seen in our results (Figure 23). The model showed that the OI predict the areas of high ossification on the diaphysis and epiphysis, and how the PTHrP and hydrostatic stresses helped with the cartilage growth and maintenance.

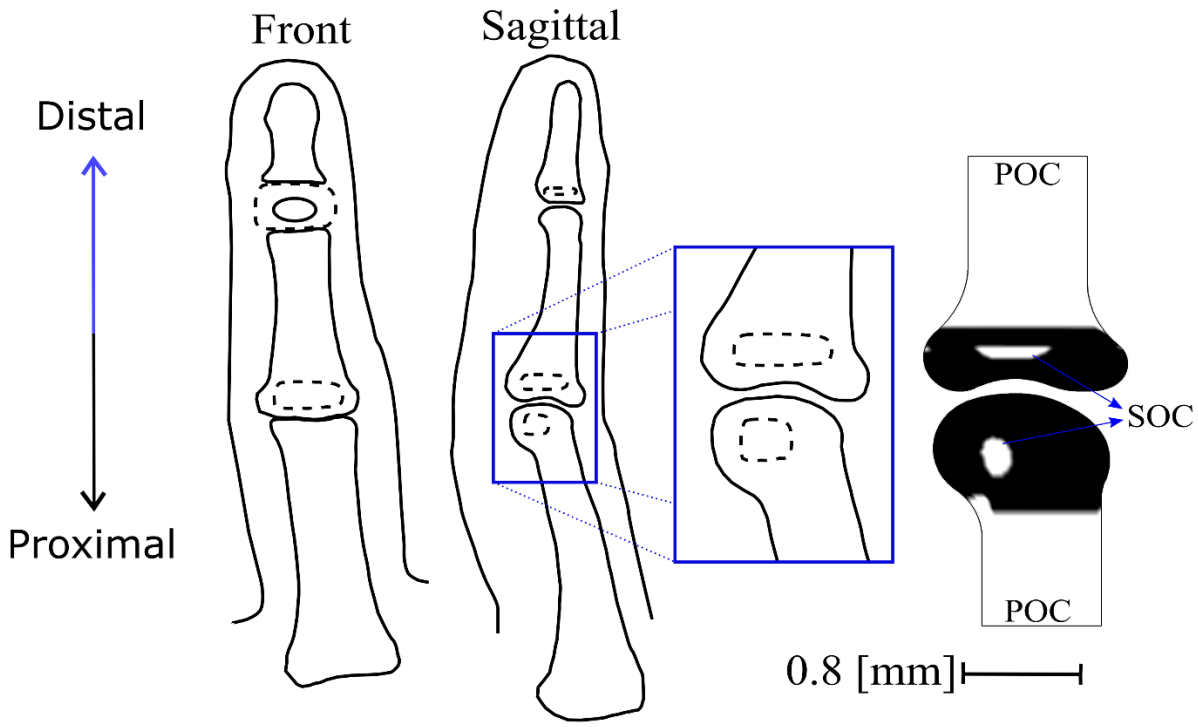

Figure 23. Comparison with a schematic draw of the Secondary Ossification Centers (SOC) [Authors]

For this model, the OI computation was based on the one proposed by Carter and Wong (1988)[15]. They established that the OI is calculated based on the octahedral shear stress and the hydrostatic stress multiplied by an empirical constant *K*. The values of the multiplier *k* for the octahedral stress was 1 and for the hydrostatic stress 0.7 for the proximal phalanx, while, for the distal phalanx, the *k* constant took the value of 1 for octahedral stress and -0.35 for the hydrostatic stress.

The obtained results are comparable with those from former studies, where only the endochondral ossification and OI distribution was analyzed [11, 28]. The growing plate was not taken into account due to molecular distribution as chondrocyte proliferation, structure characterization and cell differentiation that can be related.

The final shapes of the joints were compared to x-ray images of interphalangeal joints (Figure 21). The obtained joint shape agrees remarkably with the ones observed in the x-rays. Therefore, as it can be seen, this work generates some light of how the mechanical environment combined with molecular factors (molecules), influences the morphogenesis of a synovial joint development.

It is worth mentioning that dynamic hydrostatic stress, as it promotes cartilage growth, is key for joint morphogenesis. However, for a joint to achieve complex shapes, it is necessary to include the cell/tissue responses to the molecular and mechanical stimuli.

It was considered that the proper combination of stimuli produces a response necessary chondrocyte proliferation and cartilage extracellular matrix productions on specific zones, which moulds the bone diaphysis to their final congruent joint surfaces' shapes.

As limitations for this model is included the fact that this is only a 2D model, therefore only one plane of motion was included. Additionally, some simplifications were made regarding material behavior and properties. Furthermore, the molecules and the mechanical stimuli need to improve his coupling in a future model observing how the molecular distribution was affected or not by the mechanical action.

Likewise, since there is no information related to embryo movement during development, and much less in relation with the fetus finger motion, all the analyzed positions were considered to have the same weight and influence on the morphogenesis process.

Nevertheless, the presented model gives an excellent approximation of what is happening during joint development and morphogenesis and brings a new understanding of these processes, which, eventually, may lead to the development of new treatments for developmental diseases, or even prevent malformations of the fetus.

7. Conclusions

It was observed that the resulted geometry obtained from the two opposite pieces of cartilage in the fetal stage are comparable with a real interphalangeal joint. The obtained results are remarkable even though the assumptions that had to be made for simplicity's sake and computational savings.

It is viewed that during each time step, the surface of each bone rudiment change. Finally, the latest shape structure obtained from the two opposite pieces of cartilage had a high similitude with an interphalangeal joint, and it is comparable with an x-ray in Figure 21.

It was observed that a computational model can explain phenomena occurs in the human body with high accuracy. This in silico model shows how the relationship between the molecular and mechanical stimuli during the morphogenesis process in a synovial joint.

It was observed that the relation between the hydrostatic stress with the PTHrP and the Wnt molecules promote chondrocyte proliferation and cartilage growth, respectively, in the zones where we have a high concentration of both, cartilage growth is promoted. However, this computational model does not show the response or a change in the molecular distribution in regard to the mechanical stimuli.

Additionally, it was observed that during the morphogenesis, these molecules (PTHrP, Wnt) still influence the joint development, areas that correspond to chondrocyte proliferation shows the increment of the number of cells while his concentration stays stable. These molecules help to mould the shape structure during the joint morphogenesis.

Due to the concentration of the hydrostatic stress in the anterior part of the proximal bone rudiment mould into a concave shape, while the head of the distal phalanx shaped into a convex structure. This, as the result of the high concentrations of octahedral shear stress on the centre of the head surface, and the high concentration of hydrostatic stress in the opposite ends of the head surface.

Moreover, the model can also obtain the appearance of the POC and SOC by computed the OI. It was observed that thoroughly the molecular distribution of the principal molecules and the mechanical stress distribution within the developing bone form the POC and SOC. In spite of not considered the effect of the growing plate during the analysis, the computational model has good agreement with the appearance of the POC and SOC in comparison with schematic drawings (Figure 23).

It was observed that during the ossification process, the OI concentration was variable depending on each rudiment, the proximal phalanx response to the octahedral shear stress and the distal

phalanx response to the shear stress (Figure 13). This relationship can be explained by the molecular distribution over the head of each bone rudiment, like the proximal rudiment has a high concentration of PTHrP, whereas, the head of the distal bone rudiment has a high concentration of Ihh, and the magnitude and distribution of the hydrostatic stress.

It was found that the molecular distribution doesn't change during the ossification process, we cannot observe how the appearance of the SOC in the proximal phalanx increased the Ihh concentration within the head surface. Even so, the OI shows that due to the relationship with the mechanical stimuli, predict a change in the molecular distribution that explain the emergence of the SOC.

To our knowledge, this is the first computational model able to include several aspects of joint development, such as the main molecular and mechanical stimuli that can predict successfully the final shape of a synovial joint, like an interphalangeal joint.

8. References

[1] J. G. BETTS *et al.*, *Anatomy and Physiology*. Houston, Texas: Rice University, 2013.

[2] Raj Mitra and A. Penagos, “Chapter 6: Skin, Connective Tissue, Bone, and Joints,” in *Principles of Rehabilitation Medicine*, Kansas city, Kansas: McGraw-Hill Education, 2019, pp. 1–17.

[3] G. j. Tortora and B. Derrickson, *Principles of Anatomy and Physiology*, 12th Editi. United States of America: John Wiley & Sons, Inc., 2009.

[4] W. A. Elmer, “Developmental Cues in Limb Bud Chondrogenesis,” *Collagen Relat. Res. Clin. Exp.*, vol. 2, no. 3, pp. 257–279, 1982.

[5] C. E. Nelson *et al.*, “Analysis of Hox gene expression in the chick limb bud.,” *Development*, vol. 122, no. 5, pp. 1449–66, May 1996.

[6] M. W. Hamrick, “A chondral modeling theory revisited.,” *J. Theor. Biol.*, vol. 201, no. 3, pp. 201–208, 1999.

[7] P. H. Francis-West, J. Parish, K. Lee, and C. W. Archer, “BMP/GDF-signalling interactions during synovial joint development,” *Cell Tissue Res.*, vol. 296, no. 1, pp. 111–119, 1999.

[8] M. Pacifici, E. Koyama, and M. Iwamoto, “Mechanisms of synovial joint and articular cartilage formation: Recent advances, but many lingering mysteries,” *Birth Defects Res. Part C - Embryo Today Rev.*, vol. 75, no. 3, pp. 237–248, 2005.

[9] K. M. Márquez-Flórez, J. R. Monaghan, S. J. Shefelbine, A. Ramirez-Martínez, and D. A. Garzón-Alvarado, “A computational model for the joint onset and development,” *J. Theor. Biol.*, vol. 454, pp. 345–356, 2018.

[10] R. S. Decker, E. Koyama, and M. Pacifici, “Genesis and morphogenesis of limb synovial joints and articular cartilage,” *Matrix Biol.*, vol. 39, pp. 5–10, 2014.

[11] D. J. GRAY and E. GARDNER, “Prenatal development of the human knee and superior tibiofibular joints.,” *Am. J. Anat.*, vol. 86, no. 2, pp. 235–87, Mar. 1950.

[12] E. Gardner and R. O’Rahilly, “The early development of the knee joint in staged human embryos.,” *J. Anat.*, vol. 102, no. 2, pp. 289–299, 1968.

[13] D. R. Carter, “Mechanical loading history and skeletal biology,” *J. Biomech.*, vol. 20, no. 11–12, pp. 1095–1109, 1987.

[14] D. R. Carter, P. R. Blenman, and G. S. Beauprk, “Correlations between Mechanical Stress

History and Tissue Differentiation in Initial Fracture Healing," *J. Orthop. Res.*, vol. 6, pp. 736–748, 1988.

[15] D. R. Carter and M. Wong, "The role of mechanical loading histories in the development of diarthrodial joints," *J. Orthop. Res.*, vol. 6, no. 6, pp. 804–816, 1988.

[16] E. L. Radin, D. B. Burr, B. Caterson, D. Fyhrie, T. D. Brown, and R. D. Boyd, "Mechanical Determinants of Osteoarthrosis," *Semin. Arthritis Rheum.*, vol. 21, no. 3, pp. 12–21, 1991.

[17] P. N. P. Singh *et al.*, "Precise spatial restriction of BMP signaling in developing joints is perturbed upon loss of embryo movement," *Development*, vol. 145, no. 5, p. dev153460, 2018.

[18] L. H. Brunt, J. L. Norton, J. A. Bright, E. J. Rayfield, and C. L. Hammond, "Finite element modelling predicts changes in joint shape and cell behaviour due to loss of muscle strain in jaw development," *J. Biomech.*, vol. 48, no. 12, pp. 3112–3122, 2015.

[19] O. Silva-caicedo and I. D. A. Garzón-alvarado, "Antecedentes , historia y pronóstico de la displasia del desarrollo de la cadera," *Rev. Cuba. Investig. Biomédicas*, vol. 30, no. 1, pp. 141–162, 2011.

[20] T. A. Rando and F. Ambrosio, "Regenerative Rehabilitation: Applied Biophysics Meets Stem Cell Therapeutics," *Cell Stem Cell*, vol. 22, no. 3, pp. 306–309, Mar. 2018.

[21] A. G. Márquez and D. A. Garzón-Alvarado, "Mechanical factors of osteochondral diseases," *Rev. Cuba. Investig. Biomédicas*, vol. 30, no. 1, pp. 174–193, 2011.

[22] J. Kahn *et al.*, "Muscle Contraction Is Necessary to Maintain Joint Progenitor Cell Fate," *Dev. Cell*, vol. 16, no. 5, pp. 734–743, 2009.

[23] B. Álvarez Lario, *ARTROSIS - Todo lo que necesita saber*, Primera Ed. LibrosEnRed.com, 2005.

[24] P. Buxton, C. Edwards, C. W. Archer, and P. Francis-West, "Growth/differentiation factor-5 (GDF-5) and skeletal development.," *J. Bone Joint Surg. Am.*, vol. 83-A Suppl, no. Pt 1, pp. S23–S30, 2001.

[25] P. H. Francis-West *et al.*, "Mechanisms of GDF-5 action during skeletal development.," *Development*, vol. 126, no. 6, pp. 1305–1315, 1999.

[26] J. M. Kindblom, O. Nilsson, T. Hurme, C. Ohlsson, and L. Sävendahl, "Expression and localization of Indian hedgehog (Ihh) and parathyroid hormone related protein (PTHrP) in the human growth plate during pubertal development," *J. Endocrinol.*, vol. 174, no. 2, pp. 1–6, 2002.

[27] B. St-Jacques, M. Hammerschmidt, and A. P. McMahon, “Indian hedgehog signaling regulates proliferation and differentiation of chondrocytes and is essential for bone formation,” *Genes Dev.*, vol. 13, no. 16, pp. 2072–2086, Aug. 1999.

[28] E. Zelzer and B. R. Olsen, “The genetic basis for skeletal diseases,” *Nature*, vol. 423, no. 6937, pp. 343–348, 2003.

[29] E. Koyama *et al.*, “A distinct cohort of progenitor cells participates in synovial joint and articular cartilage formation during mouse limb skeletogenesis,” *Dev. Biol.*, vol. 316, no. 1, pp. 62–73, 2008.

[30] Y. Yokouchi, H. Sasaki, and A. Kuroiwa, “Homeobox gene expression correlated with the bifurcation process of limb cartilage development,” *Nature*, vol. 353, no. 6343, pp. 443–445, Oct. 1991.

[31] T. Montavon and N. Soshnikova, “Hox gene regulation and timing in embryogenesis,” *Semin. Cell Dev. Biol.*, vol. 34, pp. 76–84, 2014.

[32] S. Kimura and K. Shiota, “Sequential changes of programmed cell death in developing fetal mouse limbs and its possible roles in limb morphogenesis,” *J. Morphol.*, vol. 229, no. 3, pp. 337–346, Sep. 1996.

[33] D. Mitrovic, “Development of the diarthrodial joints in the rat embryo,” *Am. J. Anat.*, vol. 151, no. 4, pp. 475–485, Apr. 1978.

[34] I. M. Khan, S. N. Redman, R. Williams, G. P. Dowthwaite, S. F. Oldfield, and C. W. Archer, “The Development of Synovial Joints,” *Curr. Top. Dev. Biol.*, vol. 79, no. 06, pp. 1–36, 2007.

[35] J. H. Heegaard, G. S. Beaupré, and D. R. Carter, “Mechanically modulated cartilage growth may regulate joint surface morphogenesis,” *J. Orthop. Res.*, vol. 17, no. 4, pp. 509–517, Jul. 1999.

[36] M. Giorgi, A. Carriero, S. J. Shefelbine, and N. C. Nowlan, “Mechanobiological simulations of prenatal joint morphogenesis,” *J. Biomech.*, vol. 47, no. 5, pp. 989–995, 2014.

[37] Y. Q. Yang, Y. Y. Tan, R. Wong, A. Wenden, L. K. Zhang, and A. B. M. Rabie, “The role of vascular endothelial growth factor in ossification,” *Int. J. Oral Sci.*, vol. 4, no. 2, pp. 64–68, 2012.

[38] H. Hojo, S. Ohba, and U. C. Yuichi, “Signaling pathways regulating the specification and differentiation of the osteoblast lineage,” *Regen. Ther.*, vol. 1, pp. 57–62, 2015.

[39] S. Provot and E. Schipani, “Molecular mechanisms of endochondral bone development,” *Biochem. Biophys. Res. Commun.*, vol. 328, no. 3, pp. 658–665, 2005.

[40] S. E. Usmani, M. A. Pest, G. Kim, S. N. Ohora, L. Qin, and F. Beier, “Transforming growth factor alpha controls the transition from hypertrophic cartilage to bone during endochondral bone growth,” *Bone*, vol. 51, no. 1, pp. 131–141, 2012.

[41] V. Sarin and D. Carter, “Mechanobiology and joint conformity regulate endochondral ossification of sesamoids.,” *J. Orthop. Res.*, vol. 18, no. 5, pp. 706–712, 2000.

[42] C. H. Galeano, J. M. Mantilla, and J. C. Galvis, *El método de los elementos finitos - Un enfoque teórico practico*, Universida. Bogotá, Colombia, 2016.

[43] E. Koyama *et al.*, “Synovial joint formation during mouse limb skeletogenesis: Roles of Indian hedgehog signaling,” *Ann. N. Y. Acad. Sci.*, vol. 1116, pp. 100–112, 2007.

[44] P. Dollé *et al.*, “Differential expression of genes encoding alpha, beta and gamma retinoic acid receptors and CRABP in the developing limbs of the mouse.,” *Nature*, vol. 342, no. 6250, pp. 702–5, Dec. 1989.

[45] a M. Nalin, T. K. Greenlee, and L. J. Sandell, “Collagen gene expression during development of avian synovial joints: transient expression of types II and XI collagen genes in the joint capsule.,” *Dev. Dyn.*, vol. 203, no. 3, pp. 352–362, 1995.

[46] D. R. Carter, G. S. Beaupré, M. Wong, R. L. Smith, T. P. Andriacchi, and D. J. Schurman, “The Mechanobiology of Articular Cartilage Development and Degeneration,” *Clin. Orthop. Relat. Res.*, vol. 427, no. 427, pp. S69–S77, 2004.

[47] H. A. Castro-abril, M. Lucía, and D. A. Garzón-alvarado, “Proximal femoral growth plate mechanical behavior : Comparison between different developmental stages,” *Comput. Biol. Med.*, vol. 76, pp. 192–201, 2016.

[48] J. C. V. Acosta, D. A. Garzón-Alvarado, and L. M. P. Corte, “A mechanobiological model of epiphysis structures formation,” *J. Theor. Biol.*, vol. 287, pp. 13–25, 2011.

[49] J. M. Guevara, M. A. Moncayo, J. J. Vaca-González, M. L. Gutiérrez, L. A. Barrera, and D. A. Garzón-Alvarado, “Growth plate stress distribution implications during bone development: A simple framework computational approach,” *Comput. Methods Programs Biomed.*, vol. 118, no. 1, pp. 59–68, Jan. 2015.

[50] D. A. Garzón-alvarado, J. M. García-aznar, and M. Doblaré, “Appearance and location of secondary ossification centres may be explained by a reaction – diffusion mechanism,” *Comput. Biol. Med.*, vol. 39, pp. 554–561, 2009.

[51] D. R. Carter and M. Wong, “Modelling cartilage mechanobiology,” *Philos. Trans. R. Soc. B Biol. Sci.*, vol. 358, no. 1437, pp. 1461–1471, 2003.

9. Annexes

To develop the Finite Element Method (FEM), first we have to define the equilibrium state of a planar element (Figure 24), a quadrilateral element with linear elastic and isotropic material properties, and we considering a plane strain condition. Solving $\sum \boldsymbol{M_i}$ and $\sum \boldsymbol{F_i}$ and dividing this equation by the volume ($\Delta x \Delta y \Delta z$) obtaining the matrix form in tensorial notation (Eq. 5). The $\underline{\underline{\sigma}}$ is the stress tensor, ∇ nabla is the partial differential operator and the $\underline{f}$ is the body forces.

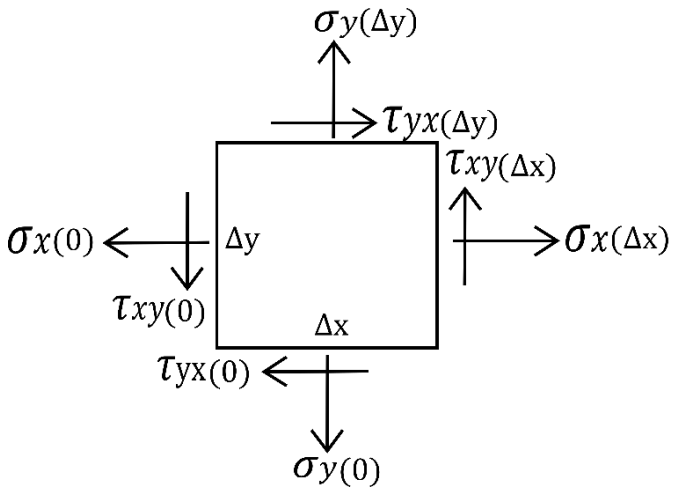

Figure 24. Infinitesimal element considering ($\Delta x \approx \Delta y \approx 0$) and ($\Delta z = 1$) [Authors]

$$\nabla \underline{\underline{\sigma}} + \underline{f} = \underline{0} \qquad \text{Eq. 5}$$

On the other hand, the relation between the stress-strain is given by the Hoke's law (Eq. 6). In this case, the stress tensor (Eq. 8) and the strain tensor (Eq. 9) will transform into a vector using Voight notation (isomorphism).

$$\underline{\underline{\sigma}} = \underline{\underline{\underline{\underline{D}}}}\, \underline{\underline{\epsilon}} \qquad \text{Eq. 6}$$

For plane strain, the material elastic matrix has a symmetric form, and is knowing as $\underline{\underline{\underline{\underline{D}}}}$ (Eq. 7).

$$\underline{\underline{\underline{\underline{D}}}} = \begin{bmatrix} \frac{E(1-\nu)}{(1-2\nu)(1+\nu)} & \frac{E\nu}{(1-2\nu)(1+\nu)} & 0 \\ \frac{E\nu}{(1-2\nu)(1+\nu)} & \frac{E(1-\nu)}{(1-2\nu)(1+\nu)} & 0 \\ 0 & 0 & \frac{E}{2(1+\nu)} \end{bmatrix} \qquad \text{Eq. 7}$$

$$\underline{\underline{\sigma}} = \begin{bmatrix} \sigma_x & \tau_{xy} \\ \tau_{yx} & \sigma_y \end{bmatrix} \rightarrow \underline{\sigma} = \begin{bmatrix} \sigma_x \\ \sigma_y \\ \tau_{xy} \end{bmatrix} \quad \text{Eq. 8}$$

$$\underline{\underline{\epsilon}} = \begin{bmatrix} \epsilon_x & \epsilon_{xy} \\ \epsilon_{yx} & \epsilon_y \end{bmatrix} \rightarrow \underline{\epsilon} = \begin{bmatrix} \epsilon_x \\ \epsilon_y \\ 2\epsilon_{xy} \end{bmatrix} = \begin{bmatrix} \epsilon_x \\ \epsilon_y \\ \gamma_{xy} \end{bmatrix} = \begin{bmatrix} \frac{du_x}{dx} \\ \frac{du_y}{dy} \\ \frac{du_x}{dy} + \frac{du_y}{dx} \end{bmatrix} \quad \text{Eq. 9}$$

All the equation becomes into a vector form, in that case, we used the basis for FEM that consist of apply residual weighted was $\underline{W}$ becomes the weighting function, $\partial\Omega$ becomes the partial domain of the problem and $\underline{\underline{\tilde{\sigma}}}$ this becomes the approximate function for the problem. In this case, it was used the tensor form of stress with the aim to show the application of the divergence theorem to the Galerkin weak form formulation. After that, for computational sakes, we used Voight notation for programming the equation in a FORTRAN subroutine solved in ABAQUS v6.13 (Dassault Systémes USA, Waltham, MA).

$$\int_{\Omega} \underline{W} \cdot \left[\nabla \cdot \underline{\underline{\tilde{\sigma}}} + \underline{f} \right] \partial\Omega = 0 \quad \text{Eq. 10}$$

$$\int_{\Omega} \underline{W} \cdot \left[\nabla \cdot \underline{\underline{\tilde{\sigma}}} \right] \partial\Omega + \int_{\Omega} \left[\underline{W} \cdot \underline{f} \right] \partial\Omega = 0 \quad \text{Eq. 11}$$

The divergence theorem was applied over the first integral form $\int_{\Omega} \underline{W} \cdot \left[\nabla \cdot \underline{\underline{\tilde{\sigma}}} \right] \partial\Omega$ and all the equation was multiplied by (-1) and obtained:

$$-\int_{\Gamma} \underline{W} \cdot \underline{\underline{\tilde{\sigma}}} \hat{n} \, \partial\Gamma + \int_{\Omega} \nabla \underline{W} : \underline{\underline{\tilde{\sigma}}} \, \partial\Omega - \int_{\Omega} \underline{W} \cdot \underline{f} \, \partial\Omega = 0 \quad \text{Eq. 12}$$

The first term in the Eq. 12, $-\int_{\Gamma} \underline{W} \cdot \underline{\underline{\tilde{\sigma}}} \hat{n} \, \partial\Gamma$ represents all the boundary conditions of the problem, this section become $-\int_{\Gamma} \underline{W} \cdot \underline{T} \, \partial\Gamma$ were $\underline{T}$ represents the traction vector over the boundary of the domain and Γ represents the contour of the problem. When the reduction ends, we used the Voight notation to transform all tensor into a vector form as we have seen on Eq. 8Eq. 9.

$$\int_{\Omega} \nabla \underline{W} \cdot \underline{\tilde{\sigma}}\, \partial\Omega - \int_{\Omega} \underline{W} \cdot \underline{f}\, \partial\Omega - \int_{\Gamma} \underline{W} \cdot \underline{T}\, \partial\Gamma = 0 \qquad \text{Eq. 13}$$

$$\int_{\Omega} \nabla \underline{W} \cdot \left[\underline{\underline{D}}\, \underline{\tilde{\epsilon}}\right]\, \partial\Omega - \int_{\Omega} \underline{W} \cdot \underline{f}\, \partial\Omega - \int_{\Gamma} \underline{W} \cdot \underline{T}\, \partial\Gamma = 0 \qquad \text{Eq. 14}$$

After it was defined the mathematical model, they need to be discretized by elements, it was used quadrilateral elements with aleatory geometry (Figure 25). Although, it was described as an approximate function for the deformation ($\underline{\epsilon}$). Further, this function $\underline{u}$ has described in terms of the shape function (N) and its displacement in x any y.

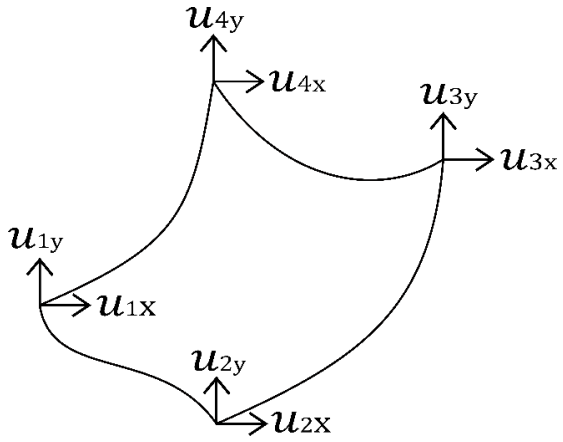

Figure 25. Quadrilateral element with the corresponding nodal displacement $u^{i}_{(x,y)}$ [Authors]

I corresponds to the respective nodal element in the x or y-direction

$$\underline{u} = ?\,? \text{ But } N = N(x, y)$$

$$u_x = N_1 u_1^x + N_1 u_1^x + N_1 u_1^x + N_1 u_1^x \qquad \text{Eq. 15}$$

$$u_y = N_1 u_1^y + N_2 u_2^y + N_3 u_3^y + N_4 u_4^y$$

As we observed in Eq. 14, the first term $\underline{W}$ this has called the principle of virtual work and represents $\delta\underline{\epsilon}$ this term has an arbitrary displacement with shape function. That becomes the partial derivatives over the shape function. Furthermore, the weight function used to describe the displacement in the strain tensor becomes the same that in the shape function N (Eq. 16), this called an isoparametric solution. Regarding the strain vector and the approximation for the displacement, is defined as the new strain vector as Eq. 19.

$$N = \begin{bmatrix} N_1 & 0 & N_2 & 0 & N_3 & 0 & N_4 & 0 \\ 0 & N_1 & 0 & N_2 & 0 & N_3 & 0 & N_4 \end{bmatrix} \quad \text{Eq. 16}$$

$$\underline{\tilde{\epsilon}} = \begin{bmatrix} \dfrac{du_x}{dx} \\ \dfrac{du_y}{dy} \\ \dfrac{du_x}{dy} + \dfrac{du_y}{dx} \end{bmatrix} \quad \text{Eq. 17}$$

$$\underline{\tilde{\epsilon}} = \begin{bmatrix} \dfrac{d}{dx}\left[N_1 u_1^x + N_1 u_1^x + N_1 u_1^x + N_1 u_1^x\right] \\ \dfrac{d}{dy}\left[N_1 u_1^y + N_2 u_2^y + N_3 u_3^y + N_4 u_4^y\right] \\ \dfrac{d}{dx}\left[N_1 u_1^y + N_2 u_2^y + N_3 u_3^y + N_4 u_4^y\right] + \dfrac{d}{dy}\left[N_1 u_1^x + N_1 u_1^x + N_1 u_1^x + N_1 u_1^x\right] \end{bmatrix} \quad \text{Eq. 18}$$

$$\underline{\tilde{\epsilon}} = \underbrace{\begin{bmatrix} \dfrac{dN_1}{dx} & 0 & \dfrac{dN_1}{dx} & 0 & \dfrac{dN_1}{dx} & 0 & \dfrac{dN_1}{dx} & 0 \\ 0 & \dfrac{dN_1}{dy} & 0 & \dfrac{dN_2}{dy} & 0 & \dfrac{dN_3}{dy} & 0 & \dfrac{dN_4}{dy} \\ \dfrac{dN_1}{dy} & \dfrac{dN_1}{dx} & \dfrac{dN_2}{dy} & \dfrac{dN_2}{dx} & \dfrac{dN_3}{dy} & \dfrac{dN_3}{dx} & \dfrac{dN_4}{dy} & \dfrac{dN_4}{dx} \end{bmatrix}}_{\underline{\underline{B}}} \underbrace{\begin{bmatrix} u_1^x \\ u_1^y \\ u_2^x \\ u_2^y \\ u_3^x \\ u_3^y \\ u_4^x \\ u_4^y \end{bmatrix}}_{\underline{u}} \quad \text{Eq. 19}$$

To continue developing the mathematical model (Eq. 14), need to change the strain vector to the new form. However, the frits term on Eq. 20, can be expressed in a different form of terms, i.e. $\nabla \underline{W} \cdot \left[\underline{\underline{D}}\ \underline{\underline{B}}\underline{u}\right] = \delta\underline{\epsilon} \cdot \underline{\tilde{\sigma}} = \delta\underline{\epsilon}^T \cdot \underline{\tilde{\sigma}} = \underline{\tilde{\sigma}}^T \cdot \delta\underline{\epsilon}$, in that way we used

$$\int_{\Omega} \nabla \underline{W} \cdot \left[\underline{\underline{D}}\ \underline{\underline{B}}\ \underline{u}\right] \partial\Omega - \int_{\Omega} \underline{W} \cdot \underline{f}\, \partial\Omega - \int_{\Gamma} \underline{W} \cdot \underline{T}\, \partial\Gamma = 0 \quad \text{Eq. 20}$$

$$\int_{\Omega} \nabla \delta\underline{\epsilon}^T \cdot \left[\underline{\underline{D}}\ \underline{\underline{B}}\ \underline{u}\right] \partial\Omega - \int_{\Omega} \delta\underline{\epsilon}^T \cdot \underline{f}\, \partial\Omega - \int_{\Gamma} \delta\underline{\epsilon}^T \cdot \underline{T}\, \partial\Gamma = 0 \quad \text{Eq. 21}$$

$$\int_{\Omega} \delta\underline{u}^T \underline{\underline{B}}^T \cdot \left[\underline{\underline{D}}\ \underline{\underline{B}}\ \underline{u}\right] \partial\Omega - \int_{\Omega} \delta\underline{u}^T \underline{\underline{N}}^T \cdot \underline{f}\, \partial\Omega - \int_{\Gamma} \delta\underline{u}^T \underline{\underline{N}}^T \cdot \underline{T}\, \partial\Gamma = 0 \quad \text{Eq. 22}$$

As we can observe in Eq. 22, the weighted function has the same properties as the shape function, nevertheless, the $\delta\underline{u}^T$ are arbitrary displacement, such in that case we can cancel in all equation obtaining:

$$\int_{\Omega} \underline{\underline{B}}^T \underline{\underline{D}}\, \underline{\underline{B}}\, \underline{u}\, \partial\Omega - \int_{\Omega} \underline{\underline{N}}^T \cdot \underline{f}\, \partial\Omega - \int_{\Gamma} \underline{\underline{N}}^T \cdot \underline{T}\, \partial\Gamma = 0 \qquad \text{Eq. 23}$$

Finally, Eq. 23, represent the mathematical model to solve element by element the discretized problem. However, as we saw in Figure 25, some discretized elements have an irregular shape to be solved in the Eq. 23, so that needs to be represented in a homogenous geometry in other coordinate system developing a geometric mapping.

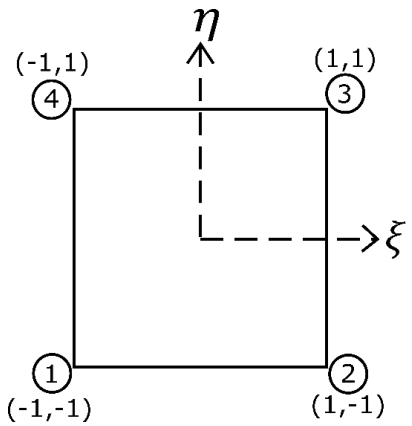

Figure 26. Quadrilateral reference element in the new coordinate system (ξ, η).

Each corner represents the node number of the element [Authors]

To the geometric mapping consist of the transform of the coordinate system were the components of the shape function N_i with $i = 1, 2, 3, 4$.

$$N = N(x, y) = N(x(\xi, \eta), y(\xi, \eta)) \qquad \text{Eq. 24}$$

$$N_1 = \frac{1}{4}(1 - \xi)(1 - \eta) \qquad \text{Eq. 25}$$

$$N_2 = \frac{1}{4}(1 + \xi)(1 - \eta) \qquad \text{Eq. 26}$$

$$N_3 = \frac{1}{4}(1 + \xi)(1 + \eta) \qquad \text{Eq. 27}$$

$$N_4 = \frac{1}{4}(1-\xi)(1+\eta) \qquad \text{Eq. 28}$$

As we saw in Eq. 24, $x = x(\xi,\eta)$ and $y = y(\xi,\eta)$ that describe the local coordinates of the element, in that case, we observed

$$\begin{aligned} u_x &= N_1(\xi,\eta)x_1 + N_2(\xi,\eta)x_2 + N_3(\xi,\eta)x_3 + N_4(\xi,\eta)x_4 \\ u_y &= N_1(\xi,\eta)y_1 + N_2(\xi,\eta)y_2 + N_3(\xi,\eta)y_3 + N_4(\xi,\eta)y_4 \end{aligned} \qquad \text{Eq. 29}$$

Such in that case, if we return to the strain vector $\left(\underline{\epsilon} = \underline{\underline{B}}\,\underline{u}\right)$ the matrix $\underline{\underline{B}}$ are the partial derivative of the shape function, however, it was defined in global coordinates (x,y) and need to be transformed in local coordinates (ξ,η). J Is known as the Jacobian of the transformation, and the differential elements on the integrated solution are represented on Eq. 32.

$$\begin{aligned} \frac{\partial N}{\partial \xi} &= \frac{\partial N}{\partial x}\frac{\partial x}{\partial \xi} + \frac{\partial N}{\partial y}\frac{\partial y}{\partial \xi} \\ \frac{\partial N}{\partial \eta} &= \frac{\partial N}{\partial x}\frac{\partial x}{\partial \eta} + \frac{\partial N}{\partial y}\frac{\partial y}{\partial \eta} \end{aligned} \qquad \text{Eq. 30}$$

$$\begin{bmatrix} \frac{\partial N}{\partial \xi} \\ \frac{\partial N}{\partial \eta} \end{bmatrix} = \underbrace{\begin{bmatrix} \frac{\partial x}{\partial \xi} & \frac{\partial y}{\partial \xi} \\ \frac{\partial x}{\partial \eta} & \frac{\partial y}{\partial \eta} \end{bmatrix}}_{J} \begin{bmatrix} \frac{\partial N}{\partial x} \\ \frac{\partial N}{\partial y} \end{bmatrix} \qquad \text{Eq. 31}$$

$$\partial x \partial y = \det J \, \partial \xi \partial \eta \qquad \text{Eq. 32}$$

Nevertheless, this Jacobian matrix we need to invert and multiplied on the other side of the equation leaving the vector $\begin{bmatrix} \frac{\partial N}{\partial x} & \frac{\partial N}{\partial y} \end{bmatrix}^T$ alone as Eq. 34. The numerical value for the invert jacobian matrix depends on the x and y global coordinate system, however, we presented the components of the Jacobian in terms of the variables x and y. the global coordinate.

$$J = \begin{bmatrix} \frac{\partial x}{\partial \xi} & \frac{\partial y}{\partial \xi} \\ \frac{\partial x}{\partial \eta} & \frac{\partial y}{\partial \eta} \end{bmatrix} = \begin{bmatrix} J_{11} & J_{12} \\ J_{21} & J_{22} \end{bmatrix} \rightarrow \; J^{-1} = \frac{1}{\det J}\begin{bmatrix} J_{22} & -J_{12} \\ -J_{21} & J_{11} \end{bmatrix} \qquad \text{Eq. 33}$$

$$\begin{bmatrix} \frac{\partial N}{\partial x} \\ \frac{\partial N}{\partial y} \end{bmatrix} = \frac{1}{\det J} \begin{bmatrix} J_{22} & -J_{12} \\ -J_{21} & J_{11} \end{bmatrix} \begin{bmatrix} \frac{\partial N}{\partial \xi} \\ \frac{\partial N}{\partial \eta} \end{bmatrix} \quad \text{Eq. 34}$$

$$J = \frac{1}{4} \begin{bmatrix} (1-\eta)(x_2 - x_1) + (1+\eta)(x_3 - x_4) & (1-\eta)(y_2 - y_1) + (1+\eta)(y_3 - y_4) \\ (1-\xi)(x_4 - x_1) + (1+\xi)(x_3 - x_2) & (1-\xi)(y_4 - y_1) + (1+\xi)(y_3 - y_2) \end{bmatrix} \quad \text{Eq. 35}$$

Finally, as we obtain the invert jacobian matrix, we return to the general equation Eq. 23 and developing the solution solving by numerical integration applying Gauss quadrature.

$$\int_{\mathrm{x}} \int_{y} \underline{\underline{B}}^T \underline{\underline{D}}\, \underline{\underline{B}}\, \underline{u}\, \partial \mathrm{x}\, \partial \mathrm{y} - \int_{x} \int_{y} \underline{\underline{N}}^T \cdot \underline{f}\, \partial \mathrm{x}\, \partial \mathrm{y} - \int_{\Gamma} \underline{\underline{N}}^T \cdot \underline{T}\, \partial \Gamma = 0 \quad \text{Eq. 36}$$

This model was programming in FORTRAN subroutines and solved in ABAQUS v6.13 (Dassault Systémes USA, Waltham, MA). This programme solved element by element solution, such in that case, we can transform the general equation into the element domain (ξ, η). Such in that case we change the Eq. 36 to the equation below:

$$\int_{-1}^{1} \int_{-1}^{1} \underline{\underline{B}}^T \underline{\underline{D}}\, \underline{\underline{B}}\, \underline{u} \det J\, \partial \xi\, \partial \eta - \int_{-1}^{1} \int_{-1}^{1} \underline{\underline{N}}^T \cdot \underline{f} \det J\, \partial \xi\, \partial \eta - \int_{\Gamma} \underline{\underline{N}}^T \cdot \underline{T}\, \partial \Gamma = 0 \quad \text{Eq. 37}$$

$$\left(\int_{-1}^{1} \int_{-1}^{1} \underline{\underline{B}}^T \underline{\underline{D}}\, \underline{\underline{B}}\, \det J\, \partial \xi\, \partial \eta \right) \underline{u} \quad \text{Eq. 38}$$

$$\int_{-1}^{1} \int_{-1}^{1} \underline{\underline{N}}^T \cdot \underline{f} \det J\, \partial \xi\, \partial \eta + \int_{\Gamma} \underline{\underline{N}}^T \cdot \underline{T}\, \partial \Gamma \quad \text{Eq. 39}$$

In this way, as we observed Eq. 38, this is known as the stiffness matrix of the element and the Eq. 39, becomes the load vector of element, obtaining the generic form of the Finite Element Method (Eq. 40). It is necessary to mentioned that the $\underline{f}$ body forces as gravity were not considered that affected our analysis formulation,

$$\underline{\underline{K}}\, \underline{u} = \underline{F} \quad \text{Eq. 40}$$

However, the early equation mentioned before (Eq. 37), need to be solved by the numerical integration (Gauss quadrature), such in that case, the numerical integration by Gauss quadrature,

is also known as Gauss-Legendre quadrature, this method allows to approximate the integral form of a soft function over the interval [-1, 1] by the next equation:

$$\int_{-1}^{1} f(\xi)\partial\xi \approx \sum_{i=1}^{n_g} w_i f(\xi_i). \qquad \text{Eq. 41}$$

Also, the Eq. 41, can be uses for a bi-dimensional problem, they can be calculated developing two (2) consecutively integration (Eq. 42) evaluating these function on the Gauss points.

$$\int_{-1}^{1}\int_{-1}^{1} f(\xi,\eta)\partial\xi\partial\eta \approx \sum_{i=1}^{n_g}\sum_{j=1}^{n_g} w_i w_j f(\xi_i,\eta_j). \qquad \text{Eq. 42}$$

Further, the next table (Table 3) present the number of points and the weights using for numerical integration by Gauss quadrature. The $\boldsymbol{P}$ represent the degree of the polynomic for which the numerical integration has $\boldsymbol{n_g}$ quadrature points for been exact. $\boldsymbol{W_i}$ are the values of the weights uses on the integral form, and $\boldsymbol{\xi_i}$ are the Gauss points were the function has to be evaluated for numerical integration [42].

Table 3. Numbers of points and weights for numerical integration using Gauss quadrature in rectangular elements[42]

$\boldsymbol{n_g}$	$\boldsymbol{W_i}$	$\boldsymbol{\xi_i}$	$\boldsymbol{P}$
1	2.000000	0.000000	1
2	1.000000	−0..5773502691896257	3
	1.000000	0.5773502691896257	
3	0.888888888	0.0000000000000000	5
	0.5555555556	−0.7745966692414834	
	0.5555555556	0.7745966692414834	
⋮	⋮	⋮	⋮

Furthermore, the stiffness matrix needs to be evaluated in all his components replaces by that Gauss points as we seen in Eq. 43. Furthermore, we presented the geometry obtained from early researches of the group [9], the boundary conditions implemented in the computational model and the post processing data for the stress analysis.

$$\left(\int_{-1}^{1}\int_{-1}^{1} \underline{\underline{B}}^T \underline{\underline{D}}\,\underline{\underline{B}}\ \det J\ \partial\xi\ \partial\eta\right)\underline{u} = \left(\sum_{i=1}^{n_g}\sum_{j=1}^{n_g} \underline{\underline{B}}^T \underline{\underline{D}}\,\underline{\underline{B}}\ \det J\ w_i w_j\right)\underline{u} \qquad \text{Eq. 43}$$

Finally, the FORTRAN subroutine developed has solved with ABAQUS v6.13 (Dassault Systémes USA, Waltham, MA), this software developed a method called Newton Raphson solution. This programme solves nonlinear problems, in this case, the programme solution need two variables called the tangent matrix (AMATRIX) and the residual vector (RHS). In the next figure (Figure 27) presents the graphical solution for the implementation of Newton-Raphson method over one-dimension variable.

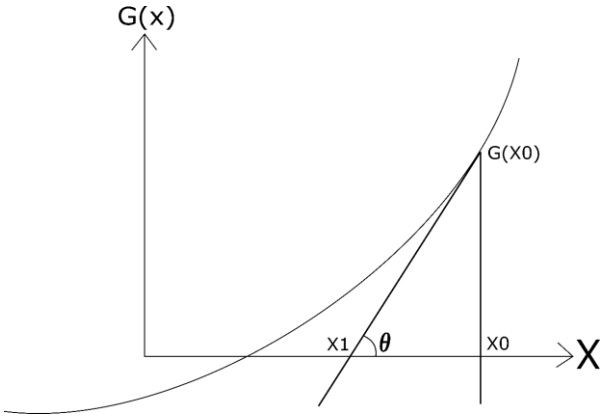

Figure 27. Newton Raphson diagram to explain ABAQUS software solution procedure [Authors]

The solution is determine by the interception with the X-axis and the curve function. Hence, the graphical solution can be expressed as the next equations. However, the tangent line becomes the derivative function evaluating in the point (X0). In this case, the parameter (X0) becomes the started point of the problem, and becomes the displacement we want to find it ($\underline{u}$), and the function $G'(X0)$ becomes the stiffness matrix of the element ($\underline{\underline{K}}$), because is the unique term that multiply the displacements, and finally, the $G(X0)$ (residual vector) becomes the stiffness matrix multiplying the displacements $\underline{\underline{K}}\,\underline{u}$. The programme need this two variables to solve the problem by the Newton Raphson method.

$$\tan\theta = \frac{G(X0)}{X1 - X0} \rightarrow G'(X0) = \frac{G(X0)}{X1 - X0} \qquad \text{Eq. 44}$$

$$G'(X0)(X1 - X0) = G(X0) \qquad \text{Eq. 45}$$